Ministère de l'Enseignement Supérieur et de la Recherche Scientifique

Université Hassiba Benbouali de Chlef

Faculté de Technologie

Département d'Electrotechnique

THÈSE

Présentée pour l'obtention du diplôme de

DOCTORAT

Filière : Électrotechnique

Spécialité : Réseaux Electriques

Par

Yahia Mohamed Amine NEDJAR

Thème :

Modélisation d'un système composé d'une décharge à barrières diélectriques dans un mélange CH_4 /Ar et une pile à combustible SOFC

« Modeling of a System Comprising a Dielectric Barrier Discharge in a CH_4/Ar Mixture and a SOFC Fuel Cell »

Soutenue le **22/02/2026**, devant le jury composé de :

Rachid TALEB	Professeur	Université Hassiba Benbouali de Chlef	Président
Mohamed MOSTEFAOUI	MCA	Université Hassiba Benbouali de Chlef	Directeur de thèse
Djilali BENYOUCEF	Professeur	Université Hassiba Benbouali de Chlef	Co- Directeur de thèse
Hocine TEBANI	MCA	Université Hassiba Benbouali de Chlef	Examinateur
Aicha AISSA BOKHTACHE	MCA	Université Hassiba Benbouali de Chlef	Examinateur
Abdlatif GUADOUM	MCA	Université Kasdi Merbah Ouargla	Examinateur
Abdelkader KANSAB	Professeur	Université Hassiba Benbouali de Chlef	Invité

Dedication

This work is lovingly dedicated to my parents, whose endless love, sacrifices, and encouragement have been the foundation of all my achievements.

To my brother and sisters, for their constant support, companionship, and faith in me through every step of this journey.

To my friends, whose presence, kindness, and understanding have brought light and balance to my life.

To all those who hold a special place in my heart, your love and inspiration have given meaning to my efforts.

And to everyone who has helped me, whether from near or far, your guidance, generosity, and encouragement have truly made the difference.

Yahia Mohamed Amine Nedjar

Acknowledgements

First and foremost, I would like to thank **Almighty God** for granting me the strength, perseverance, and patience to accomplish this work. Without His blessings, this achievement would not have been possible.

Completing this PhD thesis has been one of the most challenging and rewarding experiences of my life, and it would not have been possible without the guidance, support, and encouragement of many wonderful people to whom I owe my deepest gratitude.

I would like to express my sincere appreciation to my supervisor, **Dr. Mostefaoui Mohamed**, for his continuous guidance, invaluable advice, and patient supervision throughout this research. His deep knowledge, insightful comments, and constant encouragement have been instrumental in shaping this work and in helping me grow as a researcher.

My heartfelt thanks also go to my co-supervisor, **Prof. Djilali Benyoucef**, for his valuable assistance, thoughtful suggestions, and continuous availability whenever I needed advice. His scientific insight and friendly support made a great difference in the progress of this study.

I extend my special thanks to my **family** for their endless love, encouragement, and patience. You have been my foundation and source of strength through every challenge and success. Your belief in me gave me the courage to keep pushing forward even when things became difficult.

To my **friends and colleagues**, thank you for your constant support, stimulating discussions, and the moments of laughter that made the long hours of research more bearable.

Finally, I express my deepest gratitude to everyone who, directly or indirectly, contributed to this work. This thesis stands as a reflection of all the encouragement, kindness, and support I have received along the way.

Scientific works

List of publication:

1. N. Y. M. Amine, M. Mohamed, and B. Djilali, “Investigation of Ar/CH_4 Mixtures in Dielectric Barrier Discharge: A Simulation Approach for Hydrogen Production,” Bull. Chem. React. Eng. Catal., vol. 20, no. 3, pp. 458–470, Oct. 2025, doi: 10.9767/bcrec.20352.
2. Y. M. A. Nedjar, M. Mostefaoui, and D. Benyoucef, “One-dimensional fluid modeling of methane dissociation in dielectric barrier discharge: Impact of voltage and dielectric constant,” PPT, vol. 12, no. 1, pp. 10–15, Aug. 2025, doi: 10.14311/ppt.2025.1.10.

Conference Participation:

1. Y. M. A. Nedjar, M. Mostefaoui, and D. Benyoucef, Modeling of Hydrogen production using dielectric barrier discharge, The Sixth International Conference on Electrotechnics (ICEL’23)
2. Y. M. A. Nedjar, M. Mostefaoui, and D. Benyoucef, Two-dimensional simulation of dielectric barrier discharge in argon gas at atmospheric pressure, the first international Conference on Advances in Electronics,Control and Computer Technology (ICAECCT’23).
3. Y. M. A. Nedjar, M. Mostefaoui, and D. Benyoucef, Investigating Hydrogen Generation in Dielectric Barrier Discharge with Ar/NH3 Mixture using a 1D Fluid Model, The International Conference on the Green Solutions in the oil and gas industry sector (ICGS2025)
4. Y. M. A. Nedjar, M. Mostefaoui, and D. Benyoucef, Modeling and Analysis of CH_4 Plasma Characteristics in a Dielectric Barrier Discharge Using a 2D Fluid Approach, 3rd NATIONAL CONFERENCE ON MATERIALS SCIENCES AND ENGINEERING (MSE’2

Abstract

The transition toward sustainable energy systems requires the development of efficient and environmentally friendly technologies for hydrogen production and utilization. Hydrogen, with its high energy density and clean electrochemical conversion into electricity in fuel cells, represents a promising energy carrier for future transportation, power generation, and industrial applications. However, conventional production methods remain energy-intensive and carbon-dependent, motivating the investigation of alternative approaches.

Non-thermal plasmas, particularly dielectric barrier discharges (DBDs), offer a promising route for methane conversion and hydrogen production under near-ambient conditions without external heating. In this work, a comprehensive fluid-based plasma model was developed to investigate the behavior of an Ar/CH_4 dielectric barrier discharge. The model incorporates electron energy kinetics, detailed plasma chemistry, and self-consistent transport equations for charged species and electric fields. Parametric simulations were performed to analyze the influence of applied voltage, frequency, and gas composition on discharge dynamics, radical formation, methane conversion, and hydrogen yield. The results demonstrate that argon addition enhances plasma stability and electron density through metastable-assisted processes, improving hydrogen selectivity at intermediate mixing ratios.

In a complementary investigation, hydrogen utilization was examined through a Multiphysics model of an anode-supported SOFC. The coupled analysis of mass transport, electrochemical reactions, and thermal effects provided insights into the influence of fuel composition, stoichiometric ratio, and operating temperature on electrochemical performance. The results highlight the sensitivity of cell efficiency and current distribution to hydrogen availability and operating conditions.

Overall, this thesis presents two complementary modeling investigations addressing key stages of the hydrogen energy pathway: plasma-assisted production and electrochemical conversion. Although developed independently, these studies contribute to a broader understanding of hydrogen-based energy technologies and support the advancement of cleaner energy systems.

Keywords: Hydrogen, Fluid Model, Methane Conversion, Dielectric Barrier Discharge (DBD), Non-thermal Plasma, Plasma Chemistry, Solid Oxide Fuel Cell (SOFC).

الملخص

يقتضي التحول العالمي نحو أنظمة طاقوية مستدامة تطوير تقنيات فعّالة وصديقة للبيئة لإنتاج الهيدروجين واستغلاله. ويُعدّ الهيدروجين ناقلاً طاقوياً واعداً نظراً لكثافته الطاقوية العالية وإمكانية تحويله الكهروكيميائي النظيف إلى طاقة كهربائية داخل خلايا الوقود، حيث يكون الماء الناتج الأساسي عن هذه العملية. غير أنّ تقنيات الإنتاج التقليدية ما تزال مرتفعة الاستهلاك للطاقة وتعتمد بدرجة كبيرة على الموارد الأحفورية، مما يستدعي البحث عن مسارات بديلة أكثر استدامة وأقل أثراً بيئياً.

في هذا السياق، برزت البلازما غير الحرارية، ولا سيما تفريغ الحاجز العازل(DBD) ، كخيار واعد لتحويل الميثان وإنتاج الهيدروجين في ظروف قريبة من الضغط ودرجة الحرارة المحيطين ودون الحاجة إلى تسخين خارجي مكثف. يهدف هذا العمل إلى تطوير نموذج عددي شامل من نوع النموذج المائع لدراسة سلوك تفريغ الحاجز العازل في مزيج الأرجون/الميثان (Ar/CH_4). يعتمد النموذج على توصيف حركية طاقة الإلكترونات، وكيمياء بلازمية مفصلة، ومعادلات نقل متسقة ذاتياً للأنواع المشحونة مقترنة بمعادلات الحقول الكهربائية. وقد أُجريت دراسات بارامترية لتحليل تأثير الجهد المطبق، والتردد، وتركيب المزيج الغازي على خصائص التفريغ، وديناميكية الأنواع الفعالة، ونسبة تحويل الميثان، ومردود الهيدروجين. وأظهرت النتائج أنّ إضافة الأرجون تعزز استقرار التفريغ وكثافة الإلكترونات عبر آليات مرتبطة بالحالات شبه المستقرة، مما يؤدي إلى تحسين انتقائية إنتاج الهيدروجين عند نسب خلط متوسطة.

وفي دراسة مكمّلة، تم تناول جانب استغلال الهيدروجين من خلال تطوير نموذج متعدد الفيزياء لخلية وقود أكسيد صلب مدعومة بالأنود. وقد مكّن التحليل المقترن لانتقال الكتلة، والتفاعلات الكهروكيميائية، والتأثيرات الحرارية من تقييم تأثير تركيب الوقود، ونسبة التكافؤ(λ) ، ودرجة حرارة التشغيل على الأداء الكهروكيميائي للخلية. وأكدت النتائج أن الفواقد الأومية تمثل الآلية الغالبة في تحديد الأداء، في حين تظهر قيود انتقال الكتلة بوضوح عند التشغيل في شروط تكافؤية .($\lambda = 1$) كما أبرزت الدراسة حساسية كفاءة الخلية وتوزيع كثافة التيار لتوفر الهيدروجين وظروف التشغيل.

بصفة عامة، يقدم هذا العمل دراستين نمذجيتين متكاملتين تعالجان مرحلتين أساسيتين في سلسلة طاقة الهيدروجين، وهما الإنتاج بمساعدة البلازما غير الحرارية والتحويل الكهروكيميائي داخل خلايا الوقود. وعلى الرغم من تطوير النموذجين بشكل مستقل، فإن نتائجهما تسهم في تعميق الفهم العلمي لآليات إنتاج الهيدروجين واستغلاله، وتدعم الجهود الرامية إلى تطوير أنظمة طاقوية نظيفة وأكثر استدامة.

الكلمات المفتاحية :الهيدروجين، تحويل الميثان، تفريغ الحاجز العازل (DBD) ، البلازما غير الحرارية، كيمياء البلازما، خلية وقود الأكسيد الصلب (SOFC) ، النمذجة متعددة الفيزياء

Nomenclature

Symbol	Description
ε_0	Vacuum permittivity (F/m)
k_B	Boltzmann constant (J/K)
T_e	Electron temperature (K)
n_e	Electron density (m^{-3})
e	Elementary charge (C)
m_e	Electron mass (kg)
n_i	Ion density (m^{-3})
Λ	Plasma parameter
ns	Density of species s particles (m^{-3})
Γ_i	Particle flux of species i ($m^{-2} \cdot s^{-1}$)
Si	Net source term of species i ($m^{-3} \cdot s^{-1}$)
μ_i	Mobility of species i ($m^2 \cdot V^{-1} \cdot s^{-1}$)
Di	Diffusion coefficient of species i ($m^2 \cdot s^{-1}$)
E	Electric field vector (V/m)
εr	Relative permittivity
V	Electrostatic potential (V)
ρ	Space charge density (C/m^3)
D	Electric displacement field (C/m^2)
σ_s	Surface charge density (C/m^2)

Nomenclature

D_1, D_2	Electric displacement at adjacent media (C/m²)
D_{ij}	Binary diffusion coefficient of species i–j (m²·s⁻¹)
T	Gas temperature (K)
μ_{ij}	Reduced mass of species i–j (kg)
p	Pressure (Pa)
σ_{ij}	Collision diameter (m)
Ω_D	Collision integral for diffusion
α	Polarizability of background gas
$i_{o,a}$	Anode exchange current density (A/m²)
$i_{o,c}$	Cathode exchange current density (A/m²)
C_{H_2}, C_{H_2O}, C_t	Concentrations of H_2, H_2O, and total species (mol/m³)
F	Faraday constant (C/mol)
R	Universal gas constant (J/mol·K)
η	Overvoltage (V)
V_{cell}	Cell voltage (V)
V_{pol}	Polarization voltage loss (V)

List of Tables

List of Figures

List of Figures

Table of content

Table of content

Table of content

Table of content

General Introduction

General Introduction

The global energy transition requires innovative solutions to reduce dependence on fossil fuels and mitigate greenhouse gas emissions. Hydrogen has emerged as a promising energy carrier due to its high energy density, versatility, and clean conversion pathways. When electrochemically converted in fuel cells, hydrogen produces water as the primary by-product, making it a central component of sustainable energy strategies.

Among the various hydrogen production methods, non-thermal plasmas, particularly dielectric barrier discharges (DBDs), have attracted significant attention. Owing to their non-equilibrium characteristics, DBDs enable the activation of stable molecules such as methane at near-ambient temperatures, providing alternative routes for hydrogen generation without high thermal input. Understanding the underlying plasma physics and chemistry through numerical modeling is essential for optimizing discharge conditions and improving hydrogen selectivity and efficiency.

In parallel, solid oxide fuel cells (SOFCs) represent one of the most efficient technologies for hydrogen-based power generation. Operating at elevated temperatures, SOFCs directly convert hydrogen into electricity with high efficiency and low emissions. Their performance strongly depends on operating parameters such as temperature, fuel composition, and utilization rate, making multiphysics modeling a valuable tool for analyzing internal transport phenomena and electrochemical processes.

This thesis is therefore devoted to two complementary investigations:

• The modeling and simulation of dielectric barrier discharges in Ar/CH_4 mixtures to analyze plasma-assisted hydrogen production mechanisms.

• The modeling of anode-supported solid oxide fuel cells to evaluate electrochemical performance under hydrogen feed conditions.

The manuscript is structured as follows:

- **Chapter I** introduces the scientific background of plasmas, hydrogen energy, and fuel cells.
- **Chapter II** details the modeling framework of dielectric barrier discharges, including governing equations, plasma chemistry, and numerical approach.
- **Chapter III** presents and discusses the results of the DBD simulations, with emphasis on discharge behavior, species dynamics, methane conversion, and hydrogen yield.
- **Chapter IV** focuses on the modeling and analysis of SOFC performance, highlighting its role in efficient hydrogen utilization.

Finally, the General Conclusion summarizes the main findings and outlines perspectives for future developments, including potential system-level coupling between plasma-based hydrogen production and fuel cell technologies.

CHAPTER I: Plasma, Hydrogen, and Fuel Cells: Foundations for Clean Energy

I.1 Introduction:

The global demand for clean and sustainable energy has grown significantly in recent decades due to the depletion of fossil fuels and the urgent need to reduce greenhouse gas emissions [1][2]. Among various energy carriers, hydrogen is considered one of the most promising alternatives, owing to its high energy density and its ability to serve as a clean fuel in fuel cells [3]. Hydrogen production can be achieved through multiple pathways, including water electrolysis and thermochemical methods based on hydrocarbons, such as methane reforming [4]. Common industrial processes include steam reforming, partial oxidation of methane, and autothermal reforming [5]. However, these conventional techniques have limitations, particularly their reliance on fossil fuels and associated environmental impacts [6]. In this context, cold plasma technologies emerge as a promising approach, offering a potential complement or alternative to classical gas treatment processes [7]. Cold plasmas enable chemical reactions at low temperatures without the need for large amounts of chemical reactants. They are particularly attractive for hydrogen production and for the non-thermal conversion of methane into value-added products such as syngas and higher hydrocarbons [7]. Dielectric Barrier Discharge (DBD) reactors operate at atmospheric pressure, using energetic electrons to activate chemical reactions without significant gas heating [8]. When applied to methane, DBD plasmas can produce hydrogen, carbon monoxide, and hydrocarbons of higher molecular weight [9]. The addition of argon as a carrier gas enhances plasma stability, increases electron density, and promotes higher conversion rates [10]. Solid Oxide Fuel Cells (SOFCs) are highly efficient devices capable of directly converting hydrogen or syngas into electricity and heat [11]. In this work, the DBD plasma reactor and the SOFC are studied independently: the plasma reformer is investigated for methane conversion and hydrogen production, while the SOFC is analyzed for its performance with hydrogen-rich or syngas feeds [12]. This separate analysis provides insight into each component's behavior and potential contribution to sustainable energy production.

I.2 Plasma Theory

I.2.1 Definition and Historical Background

The term plasma was first introduced in 1923 by Irving Langmuir and Lewi Tonks [13]. Plasma is defined as a partially or fully ionized gas composed of electrons, ions, neutral atoms, and, in some cases, molecules [14]. Unlike neutral gases, plasmas exhibit collective behavior due

to long-range Coulomb interactions between charged particles, which gives rise to unique electrical and electromagnetic properties [15]. It is estimated that nearly 99% of the visible matter in the Universe exists in the plasma state, as observed in the solar corona, interstellar medium, auroras, and lightning [16-17]. For this reason, plasma is commonly referred to as the fourth state of matter [14].

I.2.2 Formation of Plasma and Phase Transition

As matter is heated, it undergoes successive phase transitions:

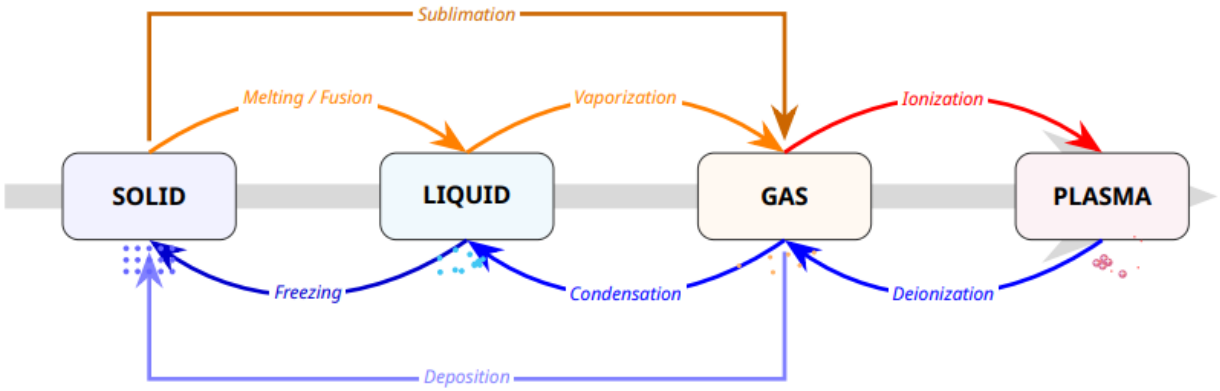

Figure I.1. Phase Transitions Between the Four States of Matter: Solid, Liquid, Gas, and Plasma.

When sufficient thermal or electrical energy is provided, electrons are detached from atoms and molecules, leading to the formation of a mixture of ions and free electrons [18]. The degree of ionization determines whether the plasma is weakly, partially, or fully ionized [19].

I.2.3 Fundamental Plasma Parameters

To characterize plasma behavior, several fundamental parameters are used:

I.2.3.1 Debye Length (λ_D):

Defines the shielding distance of electrostatic interactions in a plasma:

$$\lambda_D = \sqrt{\frac{\varepsilon_0 k_B T_e}{n_e e^2}} \quad \text{I-1}$$

where ε_0 is the vacuum permittivity, kB the Boltzmann constant, Te the electron temperature, n_e the electron density, and e the elementary charge [20].

I.2.3.2 Plasma Frequency (ω_{pe}):

The plasma frequency is a fundamental property of a plasma that describes the natural oscillation rate of electrons relative to the much heavier ions. When electrons in a plasma are displaced from their equilibrium positions, they experience a restoring force due to the electrostatic attraction of the ions, causing them to oscillate. The frequency of this oscillation is called the electron plasma frequency**,** denoted ω_{pe}, and it depends on the electron density n_e and the electron mass m_e [21]:

$$\omega_{pe} = \sqrt{\frac{n_e e^2}{\varepsilon_0 m_e}} \quad \text{I-2}$$

Where: e is the elementary charge,

ε_0 is the vacuum permittivity.

I.2.3.3 Quasi-neutrality:

In most plasmas, global charge neutrality is maintained:

$$ne \approx ni \quad \text{I-3}$$

where n_e and n_i are the electron and ion densities, respectively [15].

I.2.3.4 Plasma Parameter (Λ):

Indicates the number of particles within a Debye sphere:

$$\Lambda = \frac{4}{3}\,\pi\, n_e \,\lambda_D^3 \quad \text{I-4}$$

A medium is considered plasma if $\Lambda \gg 1$, which ensures that collective effects dominate over binary collisions [22].

I.2.4 Plasma characteristics

Plasma is characterized by several key parameters that describe its behavior and properties.

I.2.4.1 Ionization degree (α):

The ionization degree (α) represents the fraction of atoms or molecules that are ionized. In non-thermal, low-pressure plasmas, α is often very small, ranging from 10^{-6} to 10^{-3}, while in high-pressure arc plasmas it can approach unity [23].

I.2.4.2 Electron temperature (Te):

The electron temperature (Te) reflects the energy of the electron population, usually expressed in electron volts (1 eV ≈ 11,600 K). In non-thermal plasmas, Te typically ranges from 1 to 10 eV, while the neutral gas temperature (Tg) remains near room temperature or slightly elevated up to a few hundred °C [24].

I.2.4.3 Electron density (ne):

The electron density (ne) varies widely depending on the plasma type: low-pressure glow or DBD plasmas have ne values around 10^{14}–10^{18} m^{-3}, whereas atmospheric-pressure micro-discharges and streamers can reach 10^{20}–10^{24} m^{-3} locally [25].

I.2.4.4 Reduced electric field E/N:

The reduced electric field (E/N), defined as the electric field normalized by the gas number density and often expressed in Townsend units (1 Td = 10^{-21} V·m²), governs the electron energy distribution and influences reaction pathways [26].

I.2.4.5 Electron energy distribution function (EEDF):

The electron energy distribution function (EEDF)**,** which is often non-Maxwellian in non-thermal plasmas, determines the rates of excitation, ionization, and dissociation of species within the plasma [27].

Table I.1. Typical Ranges of Te, ne, Tg, and α in Thermal and Non-Thermal Plasmas.

Parameter	Thermal Plasma	Non-Thermal (Cold) Plasma
Electron Temperature (T_e)	8,000 – 50,000 K (≈ 1–5 eV)	10,000 – 100,000 K (≈ 1–10 eV)
Electron Density (n_e)	~10^{19} cm^{-3} (≈ 10^{25} m^{-3})	10^9 – 10^{13} cm^{-3} (≈ 10^{15} – 10^{19} m^{-3})
Gas / Heavy Particle Temperature (Tg)	Comparable to T_e (≈ 8,000 – 50,000 K)	Near room temperature (≈ 300 – 1,000 K)
Degree of Ionization (α)	High (≈ 0.1 – 1, often close to 1)	Very low (≈ 10^{-6} – 10^{-1})

Typical values for thermal and non-thermal plasmas illustrate these differences. Thermal plasmas have electron temperatures in the range of 8,000–50,000 K (≈ 1–5 eV), electron densities around 10^{19} cm^{-3}, gas temperatures comparable to Te, and a high ionization degree (≈ 0.1–1). In contrast, non-thermal cold plasmas exhibit higher electron temperatures of 10,000–100,000 K (≈ 1–10 eV), much lower electron densities (10^9–10^{13} cm^{-3}), gas temperatures near room temperature (≈ 300–1,000 K), and very low ionization degrees (≈ 10^{-6}–10^{-1}) [23-25].

I.2.5 Plasma generation (electrical breakdown, discharges)

Plasma generation occurs when free electrons are accelerated by an electric field to energies sufficient to ionize neutral species faster than they are lost [28]. Key phenomena in this process include:

I.2.5.1 Townsend avalanche and breakdown

Townsend avalanche and breakdown**,** where primary ionization leads to electron multiplication, and breakdown occurs when ionization growth compensates for electron losses through mechanisms such as secondary emission from electrodes or photoionization [29].

I.2.5.2 Paschen curve

The Paschen curve describes the breakdown voltage as a function of the product of pressure and electrode gap (pd), showing that for each electrode gap there exists a minimum breakdown voltage [30].

I.2.5.3 Discharge types

Different discharge types including Townsend discharge, glow discharge, arc discharge, corona, and streamer are distinguished by their spatial structure, current, and temperature characteristics [31].

I.2.6 Classification of Plasmas

Plasmas are commonly classified based on their thermodynamic properties and degree of ionization. Thermal (equilibrium) plasmas have electrons, ions, and neutrals in local thermodynamic equilibrium (LTE) and share approximately the same temperature, as in fusion plasmas, arc discharges, and the solar interior [32]. In contrast, non-thermal (cold) plasmas have electrons with much higher temperatures than ions and neutrals, allowing them to operate at or near room temperature. This makes cold plasmas suitable for industrial and environmental applications, such as surface modification, sterilization, gas treatment, and hydrogen production [33].

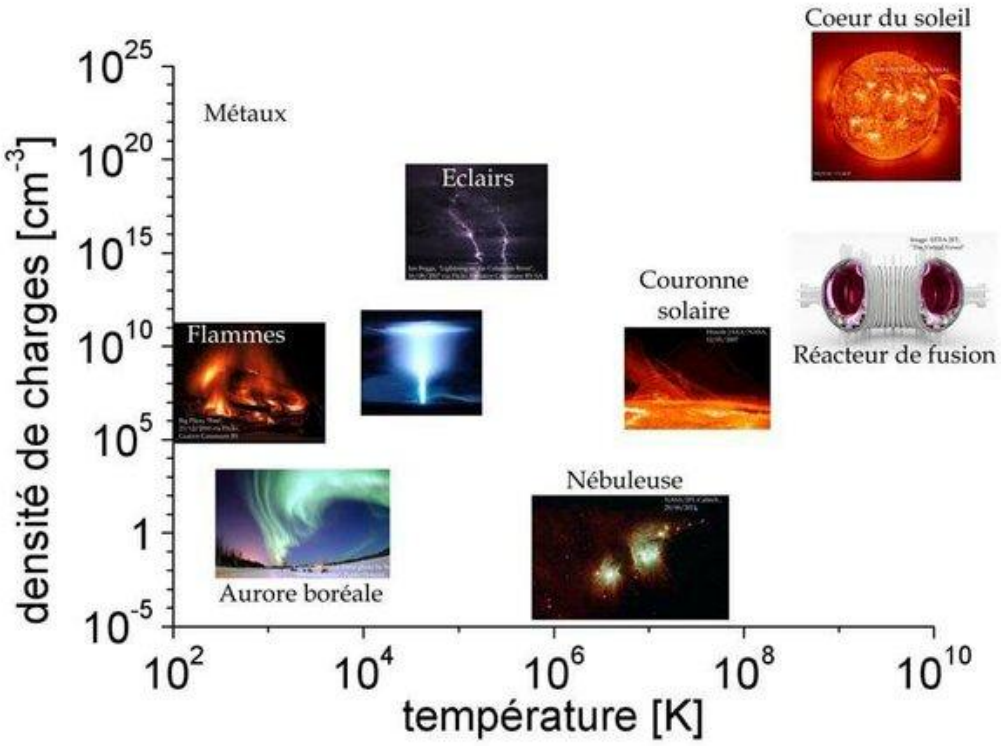

Figure I.2. Plasma Classification by Density and Electron Temperature [7].

I.3 Gas Discharges:

I.3.1.1 Generalities on Dielectric Barrier Discharges (DBD):

The term dielectric barrier discharge (DBD) refers to discharge configurations in which an electric current flow between two metallic electrodes separated by a gas and at least one dielectric layer. To sustain a current other than the displacement current across the discharge gap, the electric field must be sufficiently strong to cause gas breakdown [34, 35]. At high pressure, an increase in current between metallic electrodes typically leads to the formation of an arc regime, associated with high-temperature plasma and potential surface damage [36, 37].

The dielectric acts as a capacitor in series with the gas gap. The charge stored on its surface limits the voltage applied to the gas, preventing the transition to an arc. The accumulation of charges from the plasma on the dielectric surface reduces the effective field applied to the gas, leading to the extinction of the microdischarge [38, 39]. Being an insulator, its dielectric constant and thickness, together with the time derivative of the applied voltage dV/dt, determine the displacement current that can flow through it. This property blocks direct current (DC), making DBD discharges necessarily pulsed and requiring the use of alternating voltage (AC) to operate [40]. Common dielectric materials include glass, quartz, alumina, polymer coatings, and certain ceramics. Since current limitation by the dielectric barrier becomes less effective at very high frequencies, DBDs are typically operated within the frequency range of 1 kHz to several hundred kHz, and in some cases up to several MHz [41, 44].

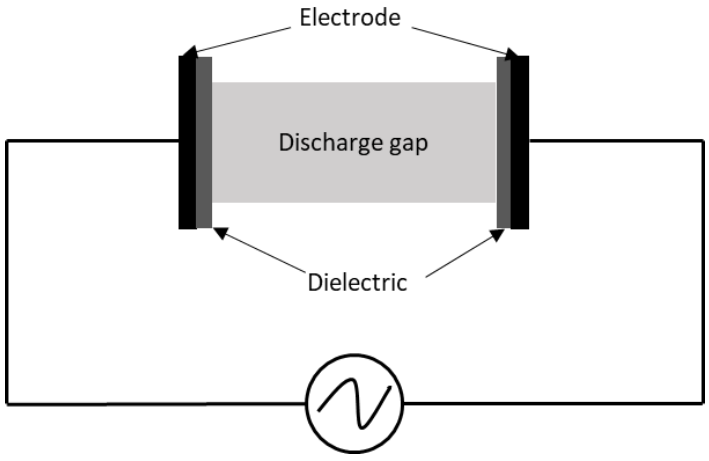

Figure I.3. Dielectric barrier discharge (DBD) configuration.

I.3.2 Principle of Operation of Dielectric Barrier Discharges (DBD)

When an AC voltage (pulsed or sinusoidal) is applied across two electrodes separated by a gas and at least one dielectric layer, the electric field in the gap increases with the applied potential. Once the field reaches the breakdown threshold of the gas (according to Paschen's law), localized microdischarges are initiated [42, 43]. These microdischarges last only a few nanoseconds and are confined to small regions of the electrode surface.

The dielectric barrier plays a crucial role in quenching microdischarges. As charges (electrons and ions) from the plasma accumulate on the dielectric surface, they locally reduce the effective electric field in the gap, preventing the transition to an arc. After extinction, the AC voltage reverses polarity, and the process repeats, creating a sequence of transient microdischarges that collectively sustain a stable non-thermal plasma [34, 35]. Since electrons reach high energies while the heavy species remain near ambient temperature, DBDs are particularly suited for applications requiring selective excitation, dissociation, or chemical activation without excessive gas heating [36, 37].

I.3.3 Historical development and applications of DBD

The concept of the DBD dates back to 1857, when Werner von Siemens first described its use for ozone generation from atmospheric air [44]. This early application rapidly led to the construction of the first ozone generators, a technology still in use today for water treatment and sterilization [34, 35].

During the 20th century, research on DBD expanded to ultraviolet (UV) radiation sources, particularly excimer lamps**.** These lamps, based on DBD excitation of rare gases and halides, provided efficient and mercury-free UV light, finding use in photolithography, surface cleaning, and medical disinfection [36, 37]. In the 1970s and 1980s, DBDs were studied for treatment of gaseous pollutants such as nitrogen oxides (NOx) and volatile organic compounds (VOCs). Their ability to generate highly reactive species (O, OH, O3) under mild conditions made them attractive for industrial exhaust cleaning and flue gas treatment [38, 39].

From the 1990s onward, DBD technology was applied in plasma display panels (PDPs) for flat-screen TVs and in plasma medicine**,** where cold DBD plasmas are used for wound healing, sterilization, and cancer treatment due to their ability to inactivate bacteria without thermal damage [40, 41]. More recently, DBD has been increasingly employed in energy and environmental technologies, including plasma-assisted hydrocarbon reforming, CO2 conversion, and hydrogen production from methane and ammonia. Its non-thermal nature allows efficient chemical activation while avoiding excessive gas heating [42, 43].

I.3.4 Typical DBD Configurations

Several electrode configurations are commonly employed depending on the application. **Coplanar configurations**, such as the parallel-plate geometry or dielectric-sandwiched arrangements, are mainly used for surface treatment. The parallel-plate setup prevents direct contact between plasma and metallic electrodes, which is useful for corrosive plasmas, while the dielectric-sandwiched configuration allows simultaneous treatment of both surfaces [34, 35].

Cylindrical configurations are more suitable for gas treatment processes, as they allow larger discharge volumes and improved homogeneity. Common dielectric materials include glass, quartz, ceramics, and polymers [36, 37, 44].

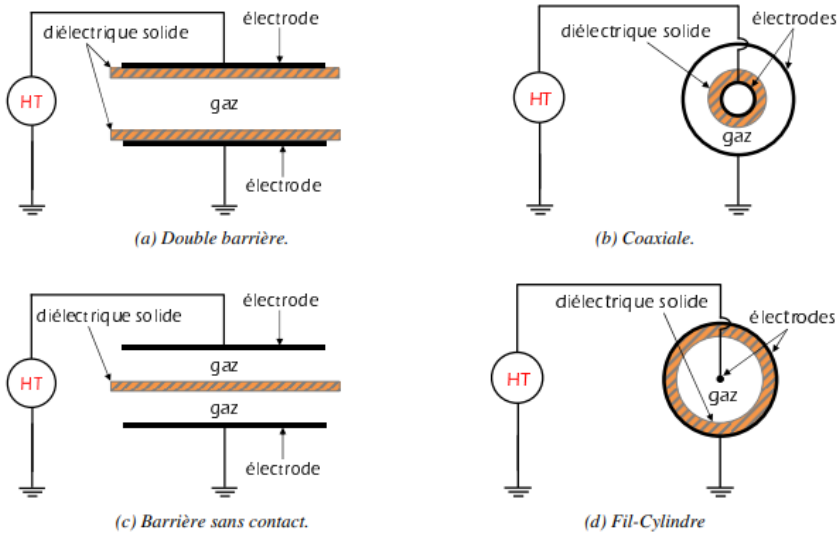

Figure I.4. Typical DBD Configurations [15].

I.3.5 Discharge Regimes

I.3.5.1 Non-self-sustained discharges:

Non-self-sustained discharges are characterized by the absence of any visible luminous phenomenon and extremely low current. In this regime, the applied voltage, typically a few tens of volts, is insufficient to induce ionization through electron-impact collisions. Conduction occurs only when an external source, such as cosmic rays, radioactive sources, or photoelectric emission, provides initial charge carriers. Since the discharge cannot maintain itself without these external contributions, it is termed non-self-sustained [45, 46].

I.3.5.2 Townsend discharges:

The Townsend regime represents the first stage of self-sustained discharges, where ionization is maintained solely by the applied voltage. In this regime, the current increases exponentially with voltage. Volume ionization is complemented by secondary electron emission at the cathode caused by ion bombardment. The current $i(x)$ at a distance x from the cathode can be expressed as:

$$i(x) = i(0)\frac{e^{ax}}{1-\gamma(e^{ax}-1)} \qquad \text{I-5}$$

where $\boldsymbol{\alpha}$ is the volumetric ionization coefficient (by electron-neutral impact) and $\boldsymbol{\gamma}$ is the secondary electron emission coefficient at the cathode. The multiplication factor is:

$$m = \gamma(e^{ax}-1) \qquad \textit{I-6}$$

When $m = 1$, the discharge becomes self-sustaining, defining the Townsend regime. At low pressures, collisions are infrequent, limiting ionization, whereas at high pressures, electrons cannot gain sufficient energy between collisions. The optimal breakdown voltage lies between these extremes, as described by Paschen's law [45, 47].

I.3.5.3 Glow discharges:

Glow discharges extend the Townsend mechanism, distinguished by the formation of significant space charges. These regions of charge imbalance between electrons and ions create

internal electric fields that sustain the discharge even if the external voltage is reduced. The arc regime, a high-current extension of glow discharge, is characterized by low sustaining voltage and elevated temperatures reaching several thousand Kelvin. Ionization in this regime primarily involves thermionic and field emission processes [45, 48].

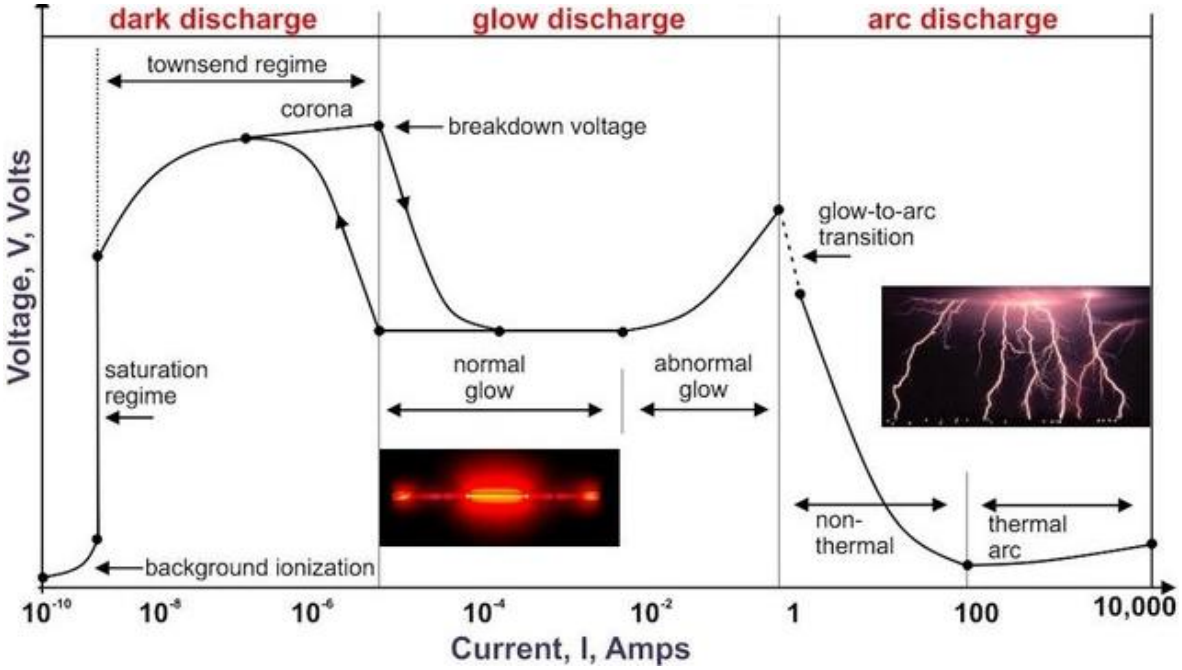

Figure I.5. Classification of Electric Discharge Regimes [15].

I.4 Hydrogen as an Energy Vector

Hydrogen has become one of the most promising energy vectors for the future of clean and sustainable energy systems [49]. Unlike primary energy sources such as fossil fuels or solar radiation, hydrogen does not exist naturally in a free state on Earth and must therefore be produced from other compounds. Once generated, it can be stored, transported, and converted into electricity or heat, offering great flexibility for integration into different sectors of the economy [50]. Its use is particularly attractive in the context of the energy transition, since hydrogen combustion or its electrochemical conversion in fuel cells results in the production of water as the only by-product, without direct carbon dioxide emissions [51]. This makes hydrogen an essential tool for decarbonization strategies and for achieving international climate objectives. Hydrogen is also considered a versatile energy carrier, capable of complementing renewable energy sources by

mitigating their intermittency through large-scale storage and power-to-gas concepts [52]. Moreover, it can be applied in hard-to-decarbonize sectors such as steel manufacturing, aviation, maritime transport, and heavy mobility, where direct electrification remains technologically or economically challenging [52].

I.4.1 Properties of Hydrogen

Hydrogen is the lightest and most abundant element in the universe, and in its molecular form (H_2) it exhibits a series of unique physical and chemical properties that make it both advantageous and challenging as an energy carrier [53]. With a molecular mass of only 2 $g \cdot mol^{-1}$, hydrogen has very high diffusivity and low density; this favors rapid dispersion in the atmosphere but complicates storage and transport, since large volumes are required to accumulate significant energy at ambient conditions [53,54]. From an energetic point of view, hydrogen has a specific energy of about 120 $MJ \cdot kg^{-1}$ (≈3× gasoline on a mass basis), while its low volumetric energy density necessitates compression, liquefaction, or advanced solid/chemical storage to meet practical volumetric energy requirements [54]. Hydrogen is characterized by a wide flammability range in air (≈4–75% by volume) and a very low minimum ignition energy (~0.02 mJ), which impose strict safety rules for handling and infrastructure [55]. In addition, hydrogen interacts with many metals and can cause embrittlement in susceptible alloys, representing a materials challenge for pipelines, tanks, and components [56]. Combustion of hydrogen yields mainly water vapor, but at high temperatures small amounts of NO_x can form from atmospheric nitrogen; thus, combustion and turbine systems must be optimized to limit NO_x formation [51].

I.4.2 Sources of Hydrogen

Hydrogen is not found freely in appreciable quantities on Earth and must be produced from other compounds such as water, hydrocarbons, or biomass; the chosen production pathway largely determines the environmental footprint and economics of the hydrogen produced [49,57]. Today the majority of industrial hydrogen is produced from fossil resources (natural gas, coal). The dominant route is steam methane reforming (SMR), where methane reacts with steam at high temperature to produce H_2 and CO, followed by a water-gas shift reaction to maximize H_2 yield a carbon-intensive process unless CO_2 is captured and stored (the “blue hydrogen” concept) [58,59].

Coal gasification is another conventional route (partial oxidation of coal to synthesis gas), but it is generally more carbon-intensive per unit H_2 than SMR and requires CCS to be compatible with deep decarbonization goals [59]. Green hydrogen — produced by water electrolysis powered by renewable electricity — offers near-zero operational CO_2 emissions and is central to long-term decarbonization roadmaps, though electrolyzer cost and renewable electricity availability remain challenges for rapid scale-up [56,60]. Biomass-based hydrogen (gasification, reforming, or biological routes) may deliver low-carbon or even net-negative options when combined with carbon capture, depending on feedstock and life-cycle choices [54]. Emerging methods (photoelectrochemical splitting, advanced electrolysis, plasma-assisted reforming) are under active investigation and pilot demonstration; these aim to improve flexibility, reduce upstream emissions, and enable distributed hydrogen production, but they require further development on efficiency and scaling [61].

I.4.3 Hydrogen Production Methods

I.4.3.1 Steam Methane Reforming (SMR)

SMR is the dominant industrial hydrogen production pathway, responsible for a large share of global supply. It proceeds at 700–1,100 °C over nickel-based catalysts, producing H_2 and CO, with a subsequent water-gas shift stage to convert CO to CO_2 and additional H_2. SMR is mature and cost-effective, but inherently carbon-intensive; coupling with carbon capture and storage is required to substantially reduce lifecycle emissions [58,59].

I.4.3.2 Coal Gasification

Coal gasification partial-oxidizes coal with steam/oxygen to produce synthesis gas (H_2 + CO) that can be shifted to maximize H_2. Historically significant in coal-rich regions, coal gasification has higher CO_2 intensity than SMR per unit H_2 and depends on effective CCS for climate compatibility [59].

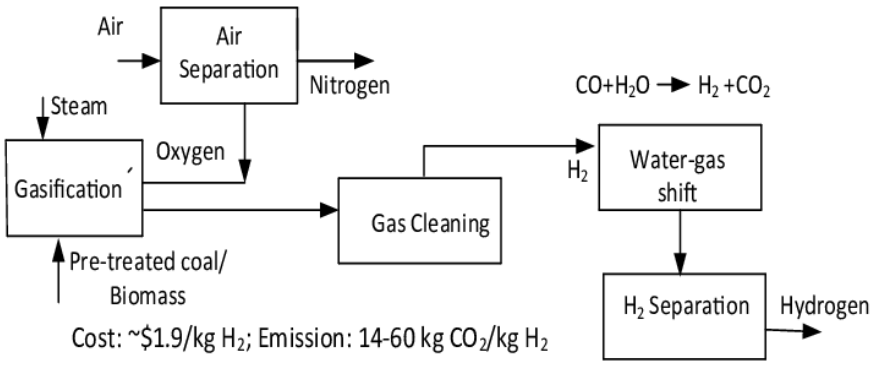

Figure I.6. Schematic Flow of a Typical Coal Gasification Process [63].

I.4.3.3 Water Electrolysis

Electrolysis represents a promising low-carbon method of hydrogen production, as it allows direct conversion of water into hydrogen and oxygen using electricity. The sustainability of this route depends on the source of electricity: when powered by renewable energy, it produces "green hydrogen." Several electrolyzer technologies are available [60,62]:

- **Alkaline Electrolyzers (AEL):** Mature, relatively inexpensive, and widely commercialized, though less dynamic in response to fluctuating renewable energy supply.

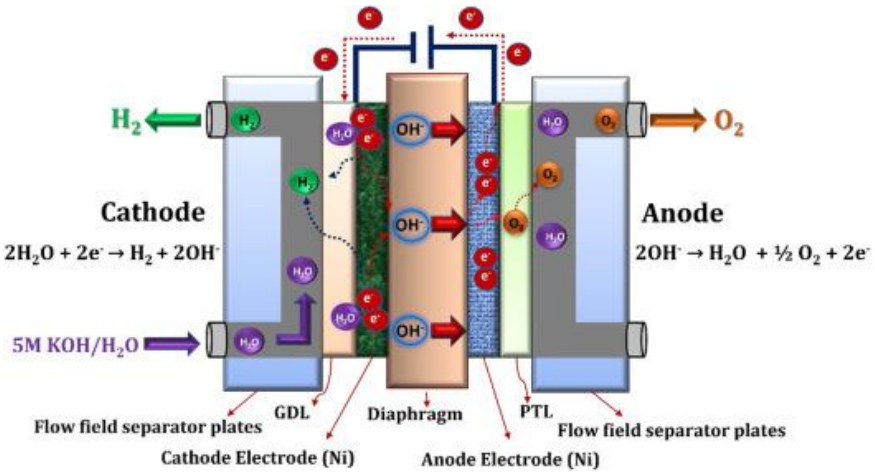

Figure I.7. Alkaline Water Electrolyzer [64].

- **Proton Exchange Membrane (PEM) Electrolyzers:** Offer higher efficiency and fast response, making them well-suited for coupling with variable renewable power sources such as solar and wind.

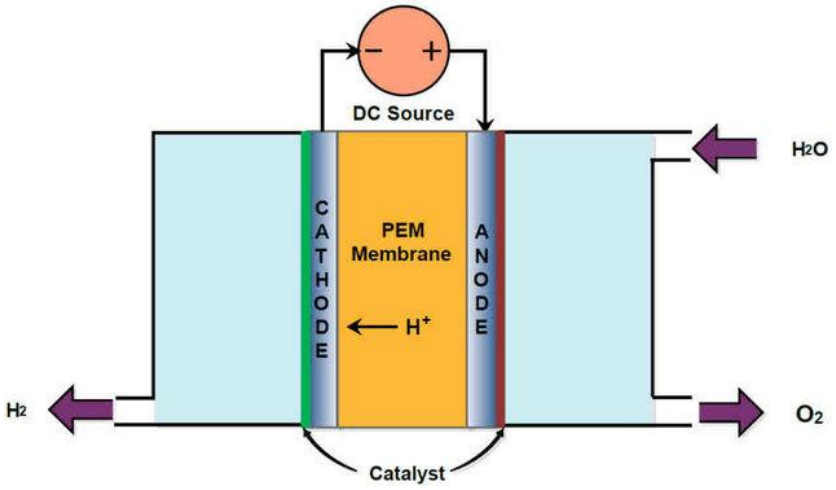

Figure I.8. Proton Exchange Membrane (PEM) Electrolyzers [65].

- **Solid Oxide Electrolyzers (SOEC):** Operate at elevated temperatures (600–900 °C), enabling high conversion efficiency and the potential for integration with waste heat, though still at an early stage of commercialization.

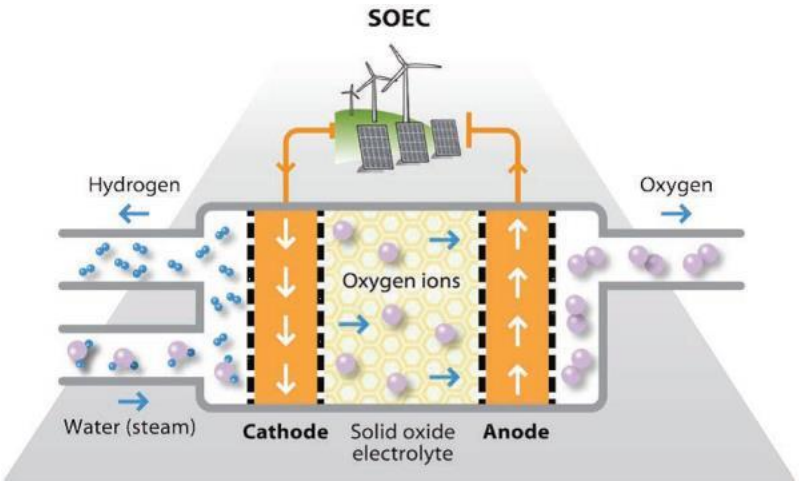

Figure I.9. Solid Oxide Electrolyzers (SOEC) [66].

I.4.3.4 Plasma-Assisted Reforming

Plasma-assisted reforming uses non-thermal plasmas (energetic electrons in a cold bulk gas) to activate stable molecules (e.g., CH_4, NH_3, H_2O) without heating the entire gas volume. DBD reactors create short-lived microdischarges that generate radicals able to dissociate methane or drive partial/dry reforming pathways. Plasma reforming is attractive for electrified, distributed hydrogen production and can be combined with catalysts (plasma-catalysis) to improve selectivity and yields; however, energy efficiency, reactor design, and scale-up remain active research topics [61,55].

I.5 Hydrogen Utilization: Fuel Cells as a Key Pathway

Fuel cells electrochemically convert hydrogen into electricity and heat with water as a primary product. PEMFCs are well suited to transport (low T, rapid start), whereas SOFCs operate at high temperature (600–1,000 °C), can internally reform hydrocarbons, tolerate CO/CO_2 in the fuel, and are attractive for stationary and cogeneration applications. Coupling plasma H_2 production with SOFCs is promising because SOFCs accept mixed feeds more readily than low-temperature fuel cells, relaxing hydrogen purification requirements; nevertheless, balance-of-plant complexity, materials cost, and long-term durability remain important deployment challenges [60,62].

I.5.1 Principle of Fuel Cell Operation

A fuel cell is an electrochemical device that directly converts the chemical energy of a fuel into electrical energy, without an intermediate combustion step. Hydrogen is the most commonly used fuel, while oxygen (or air) serves as the oxidant [60,53].

The operation relies on the spatial separation of oxidation and reduction reactions by an electrolyte that conducts ions but blocks electrons.

- **At the anode**, hydrogen is oxidized into protons and electrons:

$$H_2 \rightarrow 2H^+ + 2e\text{-}$$

The protons migrate through the electrolyte, while the electrons are forced to travel through an external circuit, producing usable electric current.

- **At the cathode**, molecular oxygen reacts with protons and incoming electrons from the external circuit to form water:

$$\frac{1}{2}O2+2H^+ +2e^- \rightarrow H_2O$$

The overall electrochemical reaction in a hydrogen fuel cell is therefore:

$$H_2 + \frac{1}{2}O2 \rightarrow H_2O + \text{energy (electrical + thermal)}$$

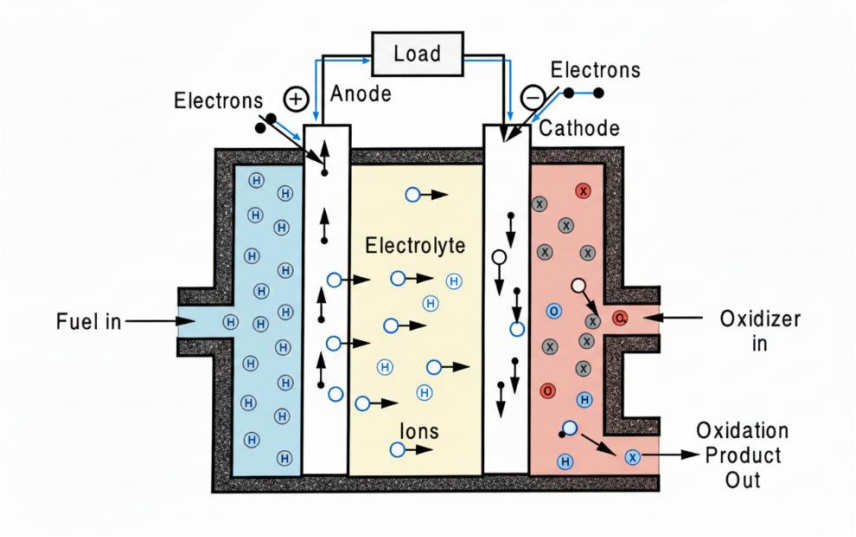

Figure I.10. Fuel Cell Working process.

I.6 Conclusion

This chapter presented the fundamental principles of plasma science and dielectric barrier discharges (DBDs), covering plasma formation, key parameters, and the distinction between thermal and non-thermal discharges. Emphasis was placed on the discharge behavior and operational characteristics of DBDs, highlighting their significance for plasma-assisted methane conversion and hydrogen production. This theoretical foundation provides the necessary context for the modeling and numerical methodology developed in Chapter II.

I.7 References

[1] Turner, J. A. (2004). Sustainable hydrogen production. *Science, 305*(5686), 972–974.

[2] Dincer, I., & Acar, C. (2015). Review and evaluation of hydrogen production methods for better sustainability. *International Journal of Hydrogen Energy, 40*(34), 11094–11111.

[3] Momirlan, M., & Veziroglu, T. N. (2005). The properties of hydrogen as fuel tomorrow in sustainable energy system for a cleaner planet. *International Journal of Hydrogen Energy, 30*(7), 795–802.

[4] Rostrup-Nielsen, J. R. (2002). Syngas in perspective. *Catalysis Today, 71*(3–4), 243–247.

[5] Rostrup-Nielsen, J. R., Sehested, J., & Nørskov, J. K. (2002). Hydrogen and synthesis gas by steam- and CO_2 reforming. *Advances in Catalysis, 47*, 65–139.

[6] Armor, J. N. (1999). The multiple roles for catalysis in the production of H_2. *Applied Catalysis A: General, 176*(2), 159–176.

[7] Fridman, A. (2008). *Plasma chemistry*. Cambridge University Press.

[8] Kogelschatz, U. (2003). Dielectric-barrier discharges: Their history, discharge physics, and industrial applications. *Plasma Chemistry and Plasma Processing, 23*(1), 1–46.

[9] Tendero, C., Tixier, C., Tristant, P., Desmaison, J., & Leprince, P. (2006). Atmospheric pressure plasmas: A review. *Spectrochimica Acta Part B: Atomic Spectroscopy, 61*(1), 2–30.

[10] Belov, I., & Naidis, G. V. (1995). Influence of argon on plasma parameters in barrier discharges. *Plasma Sources Science and Technology, 4*(4), 551–559.

[11] Singhal, S. C. (2000). Advances in solid oxide fuel cell technology. *Solid State Ionics, 135*(1–4), 305–313.

[12] Buntat, Z., Smith, R. J., & Razali, N. A. (2010). Cold plasma technology for methane reforming: A review. *International Journal of Hydrogen Energy, 35*(22), 12118–12128.

[13] Langmuir, I. (1928). Oscillations in ionized gases. *Proceedings of the National Academy of Sciences, 14*(8), 627–637.

[14] Chen, F. F. (2016). *Introduction to plasma physics and controlled fusion* (3rd ed.). Springer.

[15] Lieberman, M. A., & Lichtenberg, A. J. (2005). *Principles of plasma discharges and materials processing* (2nd ed.). John Wiley & Sons.

[16] Spitzer, L. (1962). *Physics of fully ionized gases* (2nd ed.). Interscience.

[17] Priest, E. R. (2014). *Magnetohydrodynamics of the sun*. Cambridge University Press.

[18] Raizer, Y. P. (1991). *Gas discharge physics*. Springer.

[19] Bittencourt, J. A. (2004). *Fundamentals of plasma physics* (3rd ed.). Springer.

[20] Nicholson, D. R. (1983). *Introduction to plasma theory*. John Wiley & Sons.

[21] Boyd, T. J. M., & Sanderson, J. J. (2003). *The physics of plasmas*. Cambridge University Press.

[22] Krall, N. A., & Trivelpiece, A. W. (1973). *Principles of plasma physics*. McGraw-Hill.

[23] Fridman, A., & Kennedy, L. A. (2004). *Plasma physics and engineering*. Taylor & Francis.

[24] Ben Gadri, R., Massines, F., Rabehi, A., Segur, P., & Mayoux, C. (2000). Non-thermal plasmas at atmospheric pressure: Theoretical and experimental study of a glow discharge. *Plasma Sources Science and Technology, 9*(3), 340–348.

[25] Bogaerts, A., Neyts, E., Gijbels, R., & van der Mullen, J. (2002). Gas discharge plasmas and their applications. *Spectrochimica Acta Part B: Atomic Spectroscopy, 57*(4), 609–658.

[26] Capitelli, M., Ferreira, C. M., Gordiets, B. F., & Osipov, A. I. (2000). *Plasma kinetics in atmospheric gases*. Springer.

[27] Pitchford, L. C., Hagelaar, G. J. M., & Morgan, W. L. (2007). Electron transport and rate coefficients in plasma modeling. *Plasma Processes and Polymers, 4*(7–8), 755–771.

[28] Bazelyan, E. M., & Raizer, Y. P. (1997). Spark discharge. CRC Press.

[29] Townsend, J. S. (1915). *The theory of ionization of gases by collision*. Constable & Co.

[30] Paschen, F. (1889). Ueber die zum Funkenübergang in Luft, Wasserstoff und Kohlensäure bei verschiedenen Drucken erforderliche Potentialdifferenz. *Annalen der Physik, 273*(5), 69–96. https://doi.org/10.1002/andp.18892730505

[31] Cobine, J. D. (1958). *Gaseous conductors: Theory and engineering applications*. McGraw-Hill.

[32] Mitchner, M., & Kruger, C. H. (1973). *Partially ionized gases*. Wiley.

[33] Birdsall, C. K., & Langdon, A. B. (1991). Plasma physics via computer simulation. CRC Press.

[34] Vahedi, V., & Surendra, M. (1995). A Monte Carlo collision model for the particle-in-cell method. Computer Physics Communications, 87(1–2), 179–198

[35] Eliasson, B., & Kogelschatz, U. (1991). Modeling and applications of silent discharge plasmas. *IEEE Transactions on Plasma Science, 19*(2), 309–323.

[36] Okazaki, S., Kogoma, M., Uehara, M., & Kimura, Y. (1993). Appearance of stable glow discharge in air, argon, oxygen, and nitrogen at atmospheric pressure using a 50 Hz source. *Journal of Physics D: Applied Physics, 26*(5), 889–892.

[37] Wagner, H. E., Brandenburg, R., Kozlov, K. V., Sonnenfeld, A., Michel, P., & Behnke, J. F. (2003). The barrier discharge: Basic properties and applications to surface treatment. *Vacuum, 71*(3), 417–436.

[38] Massines, F., Rabehi, A., Decomps, P., Gadri, R. B., Segur, P., & Mayoux, C. (1998). Experimental and theoretical study of a glow discharge at atmospheric pressure controlled by dielectric barrier. *Journal of Applied Physics, 83*(6), 2950–2957.

[39] Brandenburg, R., Navrátil, Z., St'ahel, P., Trunec, D., & Wagner, H. E. (2005). Time development of charge accumulation on the dielectric surface of barrier discharges in different configurations. *Czech Journal of Physics, 55*(10), 1049–1056.

[40] Roth, J. R. (1995). *Industrial plasma engineering: Volume 1: Principles*. Institute of Physics Publishing.

[41] Laroussi, M. (2002). Nonthermal decontamination of biological media by atmospheric-pressure plasmas: Review, analysis, and prospects. *IEEE Transactions on Plasma Science, 30*(4), 1409–1415.

[42] Yambe, K., Nakayama, Y., & Takashima, K. (2007). Characteristics of pulsed dielectric barrier discharge plasma and its application to environmental pollution control. *Plasma Science and Technology, 9*(5), 627–632.

[43] Zhang, Q. Z., Liu, D. W., & Wang, D. Z. (2009). Experimental study on dielectric barrier discharge for methane conversion. *Plasma Chemistry and Plasma Processing, 29*(2), 159–171.

[44] Siemens, W. (1857). Ueber die elektrostatische Induction und die Verzögerung des Stroms in Flaschendrähten. *Annalen der Physik, 178*(7), 66–122.

[45] Petrović, Z. Lj., Dujko, S., Marić, D., Malović, G., Nikitović, Ž., Sašić, O., Jovanović, Z. J., Stojanović, V., & Radmilović-Radjenović, M. (2009). Measurement and interpretation of swarm parameters and their application in plasma modelling. Journal of Physics D: Applied Physics, 42, 194002.

[46] Li, J., Ma, C., Zhu, S., Yu, F., Dai, B., & Yang, D. (2019). A review of recent advances of dielectric barrier discharge plasma in catalysis. Nanomaterials, 9(10), 1428.

[47] Griem, H. R. (1964). Plasma spectroscopy. McGraw-Hill.

[48] Nijdam, S., Teunissen, J., & Ebert, U. (2020). The physics of streamer discharge phenomena. Journal of Physics D: Applied Physics (review/tutorial).

[49] International Energy Agency. (2019). *The future of hydrogen: Seizing today's opportunities*. IEA. Retrieved from https://www.iea.org/reports/the-future-of-hydrogen

[50] U.S. Department of Energy, Office of Energy Efficiency & Renewable Energy. (n.d.). *Hydrogen basics*. Retrieved from https://www.energy.gov/eere/fuelcells/hydrogen-basics

[51] International Energy Agency. (2021). *Net zero by 2050: A roadmap for the global energy sector* (for context on hydrogen role). IEA. Retrieved from https://www.iea.org/reports/net-zero-by-2050

[52] Hydrogen Council. (2020). *Path to hydrogen competitiveness: A cost perspective*. Hydrogen Council. Retrieved from https://hydrogencouncil.com/wp-content/uploads/2020/01/Path-to-Hydrogen-Competitiveness_Full-Study-1.pdf

[53] Bicer, Y., & Dincer, I. (2018). Life cycle environmental impact assessments and comparisons of alternative fuels for clean vehicles. *Resources, Conservation and Recycling, 132*, 141–157.

[54] Züttel, A. (2003). Materials for hydrogen storage. *Materials Today, 6*(9), 24–33.

[55] Parstard, M., & Sattler, M. L. (2017).

[56] International Renewable Energy Agency (IRENA). (2020). *Green hydrogen: A guide to policy making*. IRENA. Retrieved from https://www.irena.org/publications

[57] Steele, B. C. H., & Heinzel, A. (2001). Materials for fuel-cell technologies. *Nature, 414*(6861), 345–352.

[58] Kushner, M. J. (2005). Modelling of microdischarge devices: Plasma and gas dynamics. *Journal of Physics D: Applied Physics, 38*(11), 1633–1643.

[59] Carapellucci, R. (2020). Steam, dry and autothermal methane reforming for hydrogen production. *Journal of Natural Gas Science and Engineering, 80*, 103370.

[60] Giddey, S., Badwal, S. P. S., Munnings, C., & Dolan, M. (2013). A review of solid oxide electrolysis cell technology for hydrogen production. *International Journal of Hydrogen Energy, 38*(31), 14214–14230. https://doi.org/10.1016/j.ijhydene.2013.06.089

[61] Graves, C., Ebbesen, S. D., Mogensen, M. B., & Lackner, K. S. (2019). Sustainable hydrogen production — Challenges and opportunities. *Energy & Environmental Science, 12*, 78–97.

[62] Lee, D. H., & Kim, S. H. (2023). Plasma-assisted hydrogen generation: A mechanistic review. *Journal of Energy Chemistry, 79*, 1–16.

[63] Y. Demirel, "Technoeconomics and Sustainability of Renewable Methanol and Ammonia Productions Using Wind Power-based Hydrogen," J Adv Chem Eng, vol. 5, no. 3, 2015, doi: 10.4172/2090-4568.1000128.

[64] S. Shiva Kumar and H. Lim, "An overview of water electrolysis technologies for green hydrogen production," Energy Reports, vol. 8, pp. 13793–13813, Nov. 2022, doi: 10.1016/j.egyr.2022.10.127.

[65] M. Rashid, M. K. A. Mesfer, H. Naseem, and M. Danish, "Hydrogen Production by Water Electrolysis: A Review of Alkaline Water Electrolysis, PEM Water Electrolysis and High Temperature Water Electrolysis," vol. 4, no. 3.

[66] W. Sheta, N. M. Abdeltawab, and A. Y. Shash, "Economical study for hydrogen production from seawater using renewable energy in Egypt," Materialwissenschaft Werkst, vol. 54, no. 4, pp. 371–384, Apr. 2023, doi: 10.1002/mawe.202200276.

CHAPTER II: Modeling Dielectric Barrier Discharges in Ar/CH_4 Mixtures

II.1 Introduction:

In this chapter, we present the fundamental elements of the model developed in this work. First, the relevant plasma species and chemical reactions involved in the Ar/CH_4 mixture are described. Next, we detail the physical model governing the discharge, including the electron energy distribution function, transport equations, and plasma chemistry. We then introduce the electrical representation of the DBD reactor, followed by the numerical implementation and the input data used in our simulations. This modeling framework serves as the foundation for the results and analysis presented in the subsequent chapters.

This chapter presents the modeling framework and data used to study a dielectric barrier discharge (DBD) in an Ar/CH_4 mixture. DBD behavior arises from strongly coupled physical and chemical processes, including electron kinetics, ionization, excitation, dissociation, and surface interactions, which make direct analytical treatment infeasible. Numerical modeling provides a complementary tool to experiments, enabling systematic exploration of plasma-assisted methane conversion.

Simulations allow rapid assessment of operating parameters, such as applied voltage, frequency, pressure, gas composition, and electrode configuration, on key plasma properties, including electron density, species concentrations, energy deposition, and methane-to-hydrogen conversion efficiency. Capturing these effects requires an appropriate combination of physical models, plasma chemistry, and numerical solvers due to the nonlinear coupling of charged particle densities, electric fields, and reaction kinetics.

In this work, the model incorporates the relevant plasma species and chemical reactions in the Ar/CH_4 mixture, the governing physical equations, and an electrical representation of the DBD reactor. The numerical implementation and input data are detailed to provide transparency and reproducibility.

This framework establishes the foundation for the results and analysis presented in subsequent chapters, offering insight into plasma behavior and guiding strategies to optimize methane conversion and hydrogen production.

II.2 Review of DBD Modeling Approaches

Modeling dielectric barrier discharges (DBD) requires a multiscale approach. Fast electron kinetics (nanosecond time scales, μm–mm spatial scales) coexist with much slower heavy-species chemistry, gas dynamics, and dielectric surface charging (microseconds to seconds). To capture this complexity, models range from zero-dimensional (0-D) global kinetic approaches, which describe overall species balance and power coupling, to fluid models that solve conservation equations for charged and neutral species alongside Poisson's equation for the electric field. At the highest fidelity, particle-in-cell with Monte Carlo collisions (PIC-MCC) models resolve electron energy distributions and nonlocal transport [9–11].

Global 0-D models are ideal for rapid parametric studies and reduced chemistry generation. They cannot, however, capture spatial features such as filamentation, surface charge patterns, or sheath formation, which are central to DBD behavior. Fluid (drift-diffusion) models in 1D, 2D, or 3D provide a compromise between accuracy and computational cost. They resolve electric fields, surface charge accumulation, and gas heating. Coupled with detailed chemistry, they can predict product distributions in plasma reforming and gas treatment applications [1–3]. Closure relations (mobility, diffusion, reaction rates) are obtained from Boltzmann solvers or databases (e.g., BOLSIG+, LXCat). In filament cores, they may misrepresent nonlocal or strongly non-Maxwellian electron energy distribution functions (EEDFs) [6–7].

Kinetic PIC-MCC models simulate electrons, and often ions, as particles. They include stochastic collisions and faithfully reproduce filament initiation, propagation, and electron-scale heating in microdischarges. Their computational cost limits them to small domains or short time windows [9–11]. Hybrid strategies, which combine PIC in critical regions (filaments, sheaths) with fluid descriptions elsewhere, or supplement global/fluid models with Monte Carlo-derived rates, reduce cost while retaining essential physics [6,10].

Dielectric surfaces strongly influence DBD behavior. Charge accumulation reduces the local field, quenches filaments during a half cycle, and reorganizes the discharge in the next. Accurate boundary conditions, including secondary electron emission, surface recombination, adsorption/desorption kinetics, and charge trapping are essential to reproduce reproducible filament footprints, spatial memory effects, and transitions between filamentary and homogeneous modes [2–3].

For plasma-assisted chemical processes such as methane dissociation, partial oxidation, or dry reforming, models must integrate gas-phase and surface chemistry. Large reaction sets include electron-impact reactions, vibrational excitation, radical–radical, and radical–surface processes. Sensitivity analyses and mechanism reduction keep simulations tractable while maintaining predictive capability for hydrogen and by-product yields [1,8].

Validation against experiments remains crucial. Electrical diagnostics (current/voltage waveforms, Lissajous), optical emission spectroscopy, laser diagnostics, and product analysis (GC, mass spectrometry) ensure the model captures DBD behavior, which is sensitive to electrode geometry, gas composition, pressure, dielectric properties, and applied voltage waveform [2–3].

In summary, no single model fits all DBD scenarios. The choice depends on the scientific question (microscale filament physics versus reactor-scale conversion efficiency), computational resources, and required coupling between chemistry and transport. Hybrid multi-physics strategies, validated experimentally, provide the most practical route to predictive modeling of DBD plasma reforming and plasma–catalyst systems.

II.3 Electron Energy Distribution Function (EEDF)

In non-thermal plasmas such as dielectric barrier discharges (DBDs), electrons are the most energetic species, while heavy particles (ions and neutrals) remain close to the gas temperature. The electron energy distribution function (EEDF) is therefore a key parameter, as it governs the rates of all electron-induced processes, including ionization, excitation, and dissociation [9-11]. A correct description of the EEDF is essential for obtaining reliable rate coefficients and transport parameters in plasma modeling.

The EEDF in low-temperature plasmas is generally non-Maxwellian because of the strong non-equilibrium conditions created by the oscillating electric field, frequent inelastic collisions, and confinement by dielectric surfaces [1,8]. Analytical approximations are usually insufficient, and numerical methods are required to solve the Boltzmann transport equation for electrons in a background gas mixture [6].

In this work, the EEDF is calculated using the BOLSIG+ solver, a widely used numerical tool for solving the Boltzmann equation under the two-term spherical harmonics approximation [6].

The input data for BOLSIG+ include electron collision cross sections for Ar and CH_4, which are obtained from the LXCat database [7]. For a given reduced electric field (E/N), where E is the electric field and N is the gas number density, the solver provides the steady-state EEDF, electron mobility, diffusion coefficients, and reaction rate coefficients for all included processes.

The rate coefficient for an electron-induced process is obtained by integrating the product of the corresponding cross section with the EEDF [6]:

$$k(T_e) = \int_0^\infty \sigma(\varepsilon)\ v(\varepsilon)\, f(\varepsilon)\, d\varepsilon \qquad \textit{II-1}$$

where $\sigma(\varepsilon)$ is the cross section, $v(\varepsilon)$ is the electron velocity, and $f(\varepsilon)$ is the normalized electron energy distribution function.

The shape of the EEDF strongly depends on the reduced electric field. At low E/N, the distribution resembles a Maxwellian, with most electrons having low energies. As E/N increases, the distribution shifts toward higher energies, enhancing ionization and dissociation of methane. This directly influences the production of hydrogen and other reactive species in the plasma reactor [8].

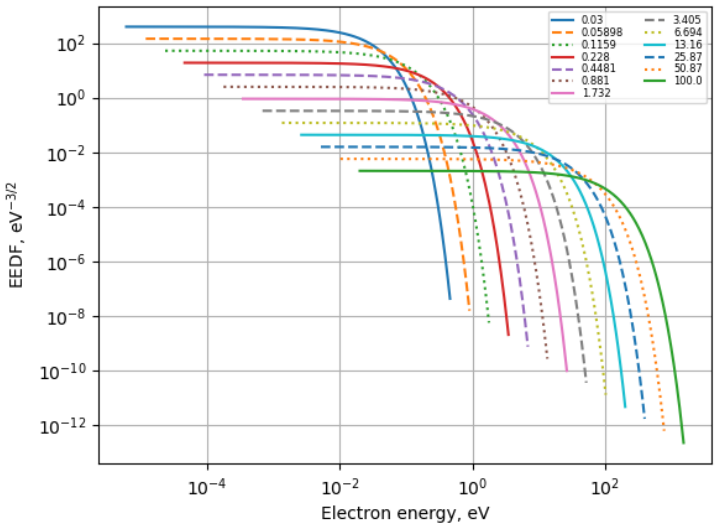

Figure II.1. typical EEDFs obtained for different values of E/N in an Ar/CH_4 mixture.

II.4 Plasma Fluid Model

The dielectric barrier discharge (DBD) considered in this work is described using a fluid model, which is widely applied for non-thermal plasma studies [9-11]. In this framework, the plasma is treated as a multi-species fluid, where the transport of charged and neutral species is governed by continuity equations coupled with the drift–diffusion approximation for particle fluxes. The source terms in these equations are determined by the chemical kinetics of the discharge, including ionization, excitation, dissociation, and recombination processes.

II.4.1 Continuity Equation

For each plasma species i (electrons, ions, neutrals), the balance equation for the particle density is written as [9]:

$$\frac{\partial n_i}{\partial t} + \nabla \cdot \Gamma_i = S_i \qquad \text{II-2}$$

where:

- n_i is the particle density of species i [m^{-3}],
- Γ_i is the particle flux [$m^{-2}s^{-1}$],
- S_i is the net source term [$m^{-3}s^{-1}$] representing creation or loss due to plasma reactions.

II.4.2 Flux Expression (Drift–Diffusion Approximation)

The flux of species i is expressed as:

$$\Gamma_i = \pm n_i \mu_i E - D_i \nabla n_i \qquad \text{II-3}$$

where:

- μ_i is the mobility of species i [$m^2V^{-1}s^{-1}$],
- D_i is the diffusion coefficient [m^2s^{-1}],

- E is the electric field vector [Vm^{-1}].

The first term corresponds to the drift motion of charged particles under the action of the electric field, while the second term represents the contribution of diffusion driven by density gradients [8-9].

II.4.3 Electron Energy Equation

Since the electron energy distribution is non-Maxwellian, an additional balance equation is introduced for the mean electron energy density n_e [6,9]:

$$\frac{\partial(n_e\varepsilon)}{\partial t} + \nabla \cdot \Gamma_\varepsilon = -e\,\Gamma_e \cdot E - \sum_j n_e k_j \Delta\varepsilon_j \qquad \text{II-4}$$

where:

- n_e is the electron density,
- ε is the mean electron energy,
- Γ_ε is the electron energy flux,
- e is the elementary charge,
- k_j is the rate coefficient of process j,
- $\Delta\varepsilon_j$ is the energy lost per collision in process j.

II.4.4 Governing Equations of the Electric Field

The transport of charged particles in a dielectric barrier discharge is strongly influenced by the spatial and temporal distribution of the electric field. In order to determine the electric field self-consistently, the electrostatic potential is obtained by solving Poisson's equation, which couples the charge densities of the plasma to the electric potential [9].

II.4.5 Poisson's Equation

The electric field inside the plasma is governed by Poisson's equation [10]:

$$\nabla \varepsilon_0 . \varepsilon_r \nabla V = \rho_s \quad \text{II-5}$$

Where **V** refers to the electrostatic potential, ε_r is the relative permittivity, and ε_0 is the vacuum permittivity.

ρ is the space charge density.

The space charge density **ρ** is computed automatically according to the plasma chemical defined in the model, utilizing the formula:

$$\rho_s = q\left(\sum_{k=1}^{N} Z_k n_k - n_e\right) \quad \text{II-6}$$

With Z_k is the electric charge, **q** is the absolute value of electronic charge.

The properties of the dielectric given by this relation:

$$D = \varepsilon_0 . \varepsilon_r E \quad \text{II-7}$$

With D refer to the electric field displacement.

II.4.6 Boundary condition:

The dielectric surfaces that are adjacent to the opening where the plasma forms are subject to surface charge accumulation as a result of the following boundary condition [2,10]:

$$-n\,.\left(D_1 - D_2\right) = \rho_s \quad \text{II-8}$$

$$\frac{d\rho_s}{dt} = n \cdot J_i + n \cdot J_e \quad \text{II-9}$$

Where ρ_s is surface charge density, $\mathbf{D_1}$ and $\mathbf{D_2}$ refer to the electric field displacement.

$\mathbf{n} \cdot \mathbf{J}_i$ is the total ion current density at the walls.

$\mathbf{n} \cdot \mathbf{J}_e$ is the total electron current density at the walls.

II.4.7 Description of model geometry:

To model the process, a one-dimensional configuration was developed, consisting of two parallel plates coated with a dielectric material having a relative permittivity of εr=10 and a thickness of 2 mm. The discharge gap, measuring 1 mm, was filled with a mixture of argon and methane, as depicted in Figure 1 [13]. This configuration is commonly used in DBD simulations to capture the essential physics while maintaining computational simplicity [3] [11] [13].

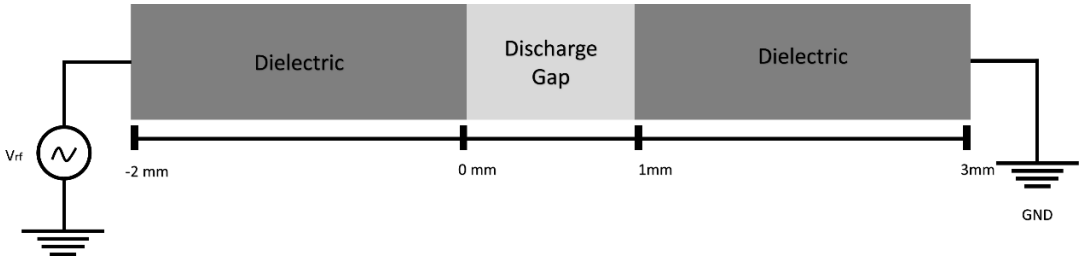

Figure II.2. 1D Geometry Model Dielectric barrier discharge reactor.

II.4.8 Simulation condition

The simulation of the dielectric barrier discharge (DBD) in an Ar/CH_4 mixture was carried out under the following physical and numerical conditions:

Table II.1. Simulation Parameters for the DBD Model.

Parameter	Value / Range
Dielectric permittivity	εr = 10
Operating pressure	p = 1 atm
Gas temperature	T = 300 K
Gas composition	Ar/CH_4
Applied voltage wave form	Sinusoidal
Applied voltage	V_0 = 5100 V
Applied Frequency	f = 40 kHz

II.4.9 Initial Value :

The initial electron density represents a small number of seed electrons present within the discharge gap domain (Figure 1):

$\mathbf{n_{e,0}}=10^6$ ($1/m^3$).

Initial mean electron energy: $\boldsymbol{\mathcal{E}}= 5$(V)

II.4.10 Time-Stepping Method:

An implicit time integration scheme based on the Backward Differentiation Formula (BDF) used to address the stiffness of the governing equations. The simulation employed an adaptive time-stepping strategy, with the initial time step set to 1×10^{-11} s. The solver dynamically adjusted the step size to accurately resolve the rapid transient behavior during breakdown and relaxation phases [12][13].

II.4.11 Spatial Discretization and Mesh:

The simulation domain, corresponding to a 1 mm discharge gap, was discretized into 200 uniform spatial nodes. This mesh density was selected based on mesh sensitivity analysis to capture steep gradients in plasma parameters, particularly near dielectric boundaries [13].

II.4.12 Solver Configuration and Convergence Criteria

The nonlinear algebraic system resulting from temporal and spatial discretization was solved using a fully coupled Newton-Raphson iteration. Within each iteration, the linear system was handled using an efficient iterative solver with appropriate preconditioning to ensure robustness and speed.

- Relative tolerance: 1×10^{-4}
- Absolute tolerance: 1×10^{-12}
- A maximum of 50 nonlinear iterations was allowed per time step.

Convergence was assessed based on the residual norm of the solution variables and conservation of charge within the domain [13] [14].

II.5 Plasma Chemistry

The plasma chemistry of an Ar/CH_4 dielectric barrier discharge involves a large number of elementary reactions, which can be grouped into several categories according to their physical and chemical role. Understanding the contribution of each reaction type is essential for interpreting the conversion of methane and the production of hydrogen [13] [15] [16].

II.5.1 Electron Impact Ionization

Ionization processes occur when energetic electrons collide with neutral species (Ar, CH_4, or their fragments), removing one electron and producing a positive ion. These reactions are crucial because they sustain the plasma by generating free electrons that maintain the discharge.

$$e + Ar \rightarrow 2e + Ar^+$$

$$e + CH_4 \rightarrow 2e + CH_4^+$$

Ionization of methane may also produce fragment ions, such as CH_3^+ or CH_2^+, which play a role in hydrocarbon growth and hydrogen release [17].

II.5.2 Electron Impact Dissociation

In dissociation reactions, the energy transferred from electrons is sufficient to break chemical bonds in methane, generating radicals such as H, CH_3, and CH_2. These radicals are highly reactive and initiate hydrocarbon chain reactions.

$$e + CH_4 \rightarrow 2e + CH_3 + H$$

$$e + CH_4 \rightarrow 2e + CH_2 + H_2$$

This pathway is the primary mechanism for methane conversion and is directly linked to hydrogen production [18].

II.5.3 Electron Impact Excitation

Excitation occurs when electrons transfer energy to neutrals without ionizing them. Excited states of argon (Ar*) or methane fragments can participate in secondary processes such as Penning ionization or stepwise ionization.

$$e + Ar \rightarrow e + Ar^*$$

These excited states act as an additional energy reservoir, which can enhance plasma reactivity [19].

II.5.4 Ion–Molecule Reactions

Once ions are formed, they interact with methane and other species through charge transfer, proton transfer, or molecular rearrangement. For instance, CH_4^+ readily reacts with methane to form CH_5^+, a key intermediate in plasma-assisted methane chemistry.

$$CH_4^+ + CH_4 \rightarrow CH_5^+ + CH_3$$

These reactions strongly influence the distribution of ion species and can contribute indirectly to hydrogen generation [20].

II.5.5 Neutral–Neutral Reactions

Radicals produced by electron impact can recombine or react with each other, leading to the formation of stable molecules such as H_2, C_2H_6, or higher hydrocarbons [15] [21].

$$H + H \rightarrow H_2$$

$$CH_3 + CH_3 \rightarrow C_2H_6$$

These reactions are important because they determine the final chemical composition of the plasma effluent, including the yield of hydrogen.

II.5.6 Recombination and Loss Processes

To ensure plasma stability, loss mechanisms such as electron–ion recombination and wall recombination of radicals are also included. These processes limit the lifetime of active species and balance the overall plasma chemistry [22].

$$CH_4^+ + e \rightarrow CH_3 + H$$

II.5.7 Species Included

This study utilizes a chemistry model that includes a thorough array of species, such as electrons, ions, radicals, and neutrals, as well as more than 100 related processes. The electron impact reactions of methane are presented in Table II.3 [23] [24], whereas the interaction between argon and methane is described in Table II.4. Methane reactions and their respective rate coefficients are presented in Table II.5.

Table II.2. Plasma Species Considered in the DBD Simulation.

Category	Species
Neutral molecules	Ar, CH_4, H_2, C_2H_6, C_2H_4
Radicals	H, CH_3, CH_2, CH, C_2H_5, C_2H_3
Positive ions	Ar^+, Ar_2^+, CH_4^+, CH_3^+, CH_2^+, CH^+, CH_5^+, $C_2H_5^+$, $C_2H_3^+$, H^+
Excited states	Ar*, Ar_2*
Electrons	e^-

Table II.3. Electron impact reactions with methane.

N°	Formula	Type	Δε (eV)	Ref
R_1	$e + CH_4 \Rightarrow e + CH_4$	Elastic	0	[24]
R_2	$e + CH_4 \Rightarrow e + CH_4$	Excitation	0.162	[24]
R_3	$e + CH_4 \Rightarrow e + CH_4$	Excitation	0.362	[24]
R_4	$e + CH_4 \Rightarrow e + CH_3 + H$	Excitation	8.8	[24]
R_5	$e + CH_4 \Rightarrow e + CH_2 + H_2$	Excitation	9.4	[24]

R_6	$e + CH_4 \Rightarrow e + CH + H_2 + H$	Excitation	12.5	[24]
R_7	$e + CH_4 \Rightarrow e + C + H_2 + H_2$	Excitation	14	[24]
R_8	$e + CH_4 \Rightarrow 2e + CH_4^+$	Ionization	12.63	[24]
R_9	$e + CH_4 \Rightarrow 2e + H + CH_3^+$	Ionization	14.25	[24]
R_{10}	$e + CH_4 \Rightarrow 2e + H_2 + CH_2^+$	Ionization	15.1	[24]
R_{11}	$e + CH_4 \Rightarrow 2e + H + H_2 + CH^+$	Ionization	19.9	[24]
R_{12}	$e + CH_4 \Rightarrow 2e + H_2 + H_2 + C^+$	Ionization	19.6	[24]
R_{13}	$e + CH_4 \Rightarrow 2e + CH_2 + H_2^+$	Ionization	20.1	[24]
R_{14}	$e + CH_4 \Rightarrow 2e + CH_3 + H^+$	Ionization	18	[24]

Table II.4. Reactions argon-methane with rate coefficient.

N°	Reaction	Rate coefficient	Ref
R_1	$Ar^+ + CH_4 \Rightarrow CH_3^+ + H + Ar$	6.32 x 10^7 m^3/(s.mol)	[25]
R_2	$Ar^* + CH_4 \Rightarrow Ar + CH_2 + 2H$	1.98 x 10^8 m^3/(s.mol)	[25]
R_3	$Ar^* + CH_4 \Rightarrow Ar + CH + H + H_2$	3.49 x 10^7 m^3/(s.mol)	[25]
R_4	$Ar^* + CH_4 \Rightarrow Ar + CH_3 + H$	3.49 x 10^7 m^3/(s.mol)	[25]
R_5	$Ar + CH_3 + H \Rightarrow CH_4 + Ar$	2.97 x 10^7 m^6/(s.mol^2)	[26]
R_7	$Ar + C_2H + H \Rightarrow C_2H_2 + Ar$	11243 m^6/(s.mol^2)	[26]
R_9	$Ar + C_2H_2 + H \Rightarrow C_2H + H_2 + Ar$	3.1878 x 10^5 m^6/(s.mol^2)	[26]
R_{10}	$Ar + C_2H_3 \Rightarrow C_2H_2 + H + Ar$	7.82 x 10^5 m^3/(s.mol)	[26]
R_{11}	$Ar^+ + CH_4 \Rightarrow CH_3^+ + H + Ar$	6.32 x 10^7 m^3/(s.mol)	[25]

R_{12}	$Ar^+ + H_2 \Rightarrow Ar^+ + H_2$	1.636 x10^8 m^3/(s.mol)	[27]
R_{13}	$Ar^+ + C_2H_2 \Rightarrow C_2H_2{}^+ + Ar$	25.29 x 10^7 m^3/(s.mol)	[27]
R_{14}	$Ar^* + Ar^* \Rightarrow e + Ar + Ar^+$	3.3734 x 10^7 m^3/(s.mol)	[28]
R_{15}	$Ar^* + Ar \Rightarrow Ar + Ar$	1807	[28]

In Table II.5, each chemical reaction is associated with a rate coefficient, which quantifies the speed at which the reaction occurs under given conditions. The rate coefficient k(T)for gas-phase reactions is commonly expressed using the modified Arrhenius equation:

$$k(T) = A\,T^n\,exp(-\frac{E}{RT}) \qquad \text{II-10}$$

where **A** is the pre-exponential factor (m^3/(s·mol) for bimolecular reactions), **n** is the temperature exponent, and **E** is the activation energy in J/mol. **T** represents the absolute temperature in Kelvin, and **R** is the universal gas constant (8.314 J/mol·K). The parameter **A** reflects the frequency of effective collisions, **n** describes the temperature dependence beyond the exponential term, and **E** indicates the minimum energy required for the reaction to proceed. These parameters together define the temperature-dependent reaction rates used in the plasma chemistry model for methane conversion and hydrogen production.

Table II.5. Chemical Reactions with Corresponding Rate Coefficients.

N°	Reaction	Rate Coefficient			Ref
		$A\left[m^3/s.mol\right]$	E[J/mol]	*n*	
R_1	$CH_4 + CH_2 \Rightarrow CH_3 + CH_3$	0.0713E−16	41988	0	[28]
R_2	$CH_4 + CH \Rightarrow C_2H_4 + H$	153E−16		–0.9	[29]
R_3	$CH_4 + H \Rightarrow CH_3 + H_2$	2.2E-26	33632	3	[30]
R_4	$CH_3 + CH_3 \Rightarrow C_2H_6$	4.66E-16		–0.37	[28]
R_5	$CH_3 + CH_3 \Rightarrow C_2H_4 + H_2$	170E−16	133030		[29]

R_6	$CH_3 + CH_3 \Rightarrow C_2H_5 + H$	0.5E−16	56540		[28]
R_7	$CH_3 + CH_2 \Rightarrow C_2H_4 + H$	0.7E−16			[28]
R_8	$CH_3 + CH \Rightarrow C_2H_3 + H$	0.5E−16			[29]
R_9	$CH_3 + C \Rightarrow C_2H_2 + H$	0.83E−16			[29]
R_{10}	$CH_3 + H_2 \Rightarrow CH_4 + H$	1.1E−26	39410	2.74	[29]
R_{11}	$CH_3 + H \Rightarrow CH_2 + H_2$	1E−16	63190		[28]
R_{12}	$CH_2 + CH_2 \Rightarrow C_2H_4$	0.017E−16			[32]
R_{13}	$CH_2 + CH_2 \Rightarrow C_2H_2 + 2H$	1.8E−16	3326		[29]
R_{14}	$CH_2 + CH_2 \Rightarrow C_2H_2 + H_2$	26.3E-16	50000		[29]
R_{15}	$CH_2 + CH_2 \Rightarrow CH_3 + CH$	4E-16	41572		[29]
R_{16}	$CH2 + CH \Rightarrow C_2H_2 + H$	0.66E−16			[31]
R_{17}	$CH_2 + C \Rightarrow C_2H + H$	0.83E−16			[31]
R_{18}	$CH_2 + H_2 \Rightarrow CH_3 + H$	0.19E−16	53212	0.17	[29]
R_{19}	$CH_2 + H \Rightarrow CH + H_2$	2.2E-16			[29]
R_{20}	$CH + CH \Rightarrow C_2H_2$	2E-16			[28]
R_{21}	$CH + C \Rightarrow C_2 + H$	0.66E−16			[29]
R_{22}	$CH + H_2 \Rightarrow CH_2 + H$	5.46E−16	16155		[29]
R_{23}	$CH + H \Rightarrow C+H_2$	1.31E−16	665		[28]
R_{24}	$C + H_2 \Rightarrow CH+H$	6.64E−16	97278		[28]
R_{25}	$CH_4^+ + CH_4 \Rightarrow CH_5^+ + CH_3$	11.5E−16			[32]

R_{26}	$CH_4^+ + H2 \Rightarrow CH_5^+ + H$	1.086E−16	–300	–0.14	[29]
R_{27}	$CH_4^+ + H \Rightarrow CH_3^+ + H_2$	0.1E−16			[29]
R_{28}	$CH_5^+ + CH_2 \Rightarrow CH_3^+ + CH_4$	9.6E−16			[29]
R_{29}	$CH_5^+ + CH \Rightarrow CH_2^+ + CH_4$	120E-16		–0.5	[29]
R_{30}	$CH_5^+ + C \Rightarrow CH^+ + CH_4$	12E-16			[29]
R_{31}	$CH_5^+ + H \Rightarrow CH_4^+ + H_2$	1.5 E-16			[29]
R_{32}	$CH_3^+ + CH_4 \Rightarrow C_2H_5^+ + H_2$	9.6E−16			[32]
R_{33}	$CH_3^+ + CH_2 \Rightarrow C_2H_3^+ + H_2$	9.9E-16			[29]
R_{34}	$CH_3^+ + CH \Rightarrow C_2H_2^+ + H_2$	123E−16		–0.5	[29]
R_{35}	$CH_3^+ + C \Rightarrow C_2H^+ + H_2$	12E-16			[29]
R_{36}	$CH_3^+ + H \Rightarrow CH_2^+ + H_2$	7E-16	87800		[29]
R_{37}	$CH_2^+ + CH_4 \Rightarrow C_2H_5^+ + H$	2.88E−16			[29]
R_{38}	$CH_2^+ + CH_4 \Rightarrow C_2H_4^+ + H_2$	5E-16			[29]
R_{39}	$CH_2^+ + CH_4 \Rightarrow C_2H_3^+ + H_2 + H$	2.64E−16			[29]
R_{40}	$CH_2^+ + CH_4 \Rightarrow C_2H_2^+ + 2H_2$	1.44E−16			[29]
R_{41}	$CH_2^+ + C \Rightarrow C_2H^+ + H$	12E−16			[29]
R_{42}	$CH_2^+ + H_2 \Rightarrow CH_3^+ + H$	7.2E-16			[33]
R_{43}	$CH_2^+ + H \Rightarrow CH^+ + H_2$	10E−16	58866		[29]

R_{44}	$CH^+ + CH_4 \Rightarrow C_2H_4^+ + H$	0.77E−16			[29]
R_{45}	$CH^+ + CH_4 \Rightarrow C_2H_3^+ + H_2$	10.57E−16			[29]
R_{46}	$CH^+ + CH_4 \Rightarrow C_2H_2^+ + H_2 + H$	1.55E−16			[29]
R_{47}	$CH^+ + CH_2 \Rightarrow C_2^+ + H_2$	10E−16			[29]
R_{48}	$CH^+ + CH \Rightarrow C_2^+ + H_2$	128E−16		–0.5	[29]
R_{49}	$CH^+ + C \Rightarrow C_2^+ + H$	12E-16			[29]
R_{50}	$CH^+ + H_2 \Rightarrow CH_2^+ + H$	10.1E−16			[29]
R_{51}	$CH^+ + H \Rightarrow C^+ + H_2$	74.75E-16	241	–0.37	[29]
R_{52}	$C^+ + CH_4 \Rightarrow C_2H_3^+ + H$	10.3E−16			[29]
R_{53}	$C^+ + CH_4 \Rightarrow C_2H_2^+ + H_2$	4.2E-16			[29]
R_{54}	$C^+ + CH_3 \Rightarrow C_2H_2^+ + H$	13E−16			[29]
R_{55}	$C^+ + CH_3 \Rightarrow C_2H^+ + H_2$	10E-16			[34]
R_{56}	$C^+ + CH_2 \Rightarrow C_2H^+ + H$	5.2E−16			[29]
R_{57}	$C^+ + CH_2 \Rightarrow CH_2^+ + C$	5.2E-16			[29]
R_{58}	$C^+ + CH \Rightarrow C_2^+ + H$	65.8E−16		–0.5	[29]
R_{59}	$C^+ + CH \Rightarrow CH^+ + C$	65.8E−16		–0.5	[29]
R_{60}	$C^+ + H2 \Rightarrow CH^+ + H$	1E−16	38579		[29]
R_{61}	$H_2^+ + CH_4 \Rightarrow CH_4^+ + H_2$	14E−16			[29]
R_{62}	$H_2^+ + CH_4 \Rightarrow CH_5^+ + H$	1.1E−16			[29]

R_{63}	$H_2^+ + CH_4 \Rightarrow CH_3^+ + H_2 + H$	22.8E−16			[29]
R_{64}	$H_2^+ + CH_2 \Rightarrow CH_2^+ + H_2.$	10E−16			[29]
R_{65}	$H_2^+ + CH_2 \Rightarrow CH_3^+ + H$	10E-16			[29]
R_{66}	$H_2^+ + CH \Rightarrow CH^+ + CH_2$	123E−16		−0.5	[29]
R_{67}	$H_2^+ + CH \Rightarrow CH_2^+ + H$			−0.5	[29]
R_{68}	$H_2^+ + C \Rightarrow CH^+ + H$	24E-16			[29]
R_{69}	$H_2^+ + H_2 \Rightarrow H_3^+ + H$	21E−16			[29]
R_{70}	$H_2^+ + H \Rightarrow H^+ + H_2$	6.4E−16			[29]
R_{71}	$H^+ + CH_4 \Rightarrow CH_4^+ + H$	15.2E−16			[29]
R_{72}	$H^+ + CH_4 \Rightarrow CH_3^+ + H_2$	22.8E-16			[29]
R_{73}	$H^+ + CH_3 \Rightarrow CH_3^+ + H$	34E-16			[29]
R_{74}	$H^+ + CH_2 \Rightarrow CH_2^+ + H$	14E−16			[29]
R_{75}	$H^+ + CH_2 \Rightarrow CH^+ + H_2$	14E-16			[29]
R_{76}	$H^+ + CH \Rightarrow CH^+ + H$	329E−16		−0.5	[29]
R_{77}	$C_2H_4^+ + H \Rightarrow C_2H_3^+ + H2$	3E-16			[29]
R_{78}	$CH_4 + C_2H_3 \Rightarrow C_2H_4 + CH_3$	2.41E-30	22860	4.02	[29]
R_{79}	$CH_3 + C_2H_6 \Rightarrow C_2H_5 + CH_4$	0.9E−30	34670	4	[29]
R_{80}	$CH_3 + C_2H_5 \Rightarrow C_2H_4 + CH_4$	0.019E−16			[28]
R_{81}	$CH_3 + C_2H_3 \Rightarrow C_2H_2 + CH_4$	8833E-16	2494	−1.5	[28]

R_{82}	$CH_2 + C_2H_3 \Rightarrow C_2H_2 + CH_3$	0.3E−16			[28]
R_{83}	$CH + C_2H_6 \Rightarrow C_2H_4 + CH_3$	4.8E−16	242.7	–0.52	[29]
R_{84}	$H + C_2H_5 \Rightarrow C_2H_6$	0.6E−16			[30]
R_{85}	$H + C_2H_5 \Rightarrow CH_3 + CH_3$	0.6E−16			[29]
R_{86}	$H + C_2H_5 \Rightarrow C_2H_4 + H_2$	0.03E−16			[32]
R_{87}	$H + C_2H_4 \Rightarrow C_2H_5$	0.14E−20	4150	1.49	[33]
R_{88}	$H + C_2H_4 \Rightarrow C_2H_3 + H_2$	2.2E-24	51220	2.53	[33]
R_{89}	$H + C_2H_3 \Rightarrow C_2H_2 + H_2$	0.332E-16			[28]
R_{90}	$H + C_2H_2 \Rightarrow C_2H + H_2$	3.8E-16	113359		[29]
R_{91}	$C_2H_5 + C_2H_5 \Rightarrow C_2H_6 + C_2H_4$	0.024E−16			[29]
R_{92}	$C_2H_5 + C_2H_5 \Rightarrow C_4H_{10}$	0.19E−16			[29]
R_{93}	$C_2H_5 + C_2H \Rightarrow C_2H_4 + C_2H_2$	0.03E−16			[28]
R_{94}	$CH_4^+ + C_2H_6 \Rightarrow C_2H_4^+ + CH_4 + H_2$	19.1E−16			[28]
R_{95}	$CH_4^+ + C_2H_4 \Rightarrow C_2H_4^+ + CH_4$	13.8E−16			[28]
R_{96}	$CH_4^+ + C_2H_4 \Rightarrow C_2H_5^+ + CH_3$	4.23E−16			[33]
R_{97}	$CH_4^+ + C_2H_2 \Rightarrow C_2H_2^+ + CH_4$	11.3E−16			[29]
R_{98}	$CH_4^+ + C_2H_2 \Rightarrow C_2H_3^+ + CH_3$	12.3E−16			[29]
R_{99}	$CH_5^+ + C_2H_4 \Rightarrow C_2H_5^+ + CH_4$	15E−16			[29]
R_{100}	$CH_5^+ + C_2H_2 \Rightarrow C_2H_3^+ + CH_4$	16E−16			[29]

R_{101}	$CH_5^+ + C_2H \Rightarrow C_2H_2^+ + CH_4$	9E−16		[29]
R_{102}	$CH_3^+ + C_2H_6 \Rightarrow C_2H_5^+ + CH_4$	14.8E−16		[29]
R_{103}	$CH_3^+ + C_2H_4 \Rightarrow C_2H_3^+ + CH_4$	3.5E−16		[29]
R_{104}	$CH_3^+ + C_2H_3 \Rightarrow C_2H_3^+ + CH_3$	51.9E−16	–0.5	[29]
R_{105}	$H_2^+ + C_2H_6 \Rightarrow C_2H_6^+ + H_2$	2.94E-16		[29]
R_{106}	$H_2^+ + C_2H_6 \Rightarrow C_2H_5^+ + H_2 + H$	13.7E−16		[29]
R_{107}	$H_2^+ + C_2H_6 \Rightarrow C_2H_4^+ + 2H_2$	23.5E−16		[29]
R_{108}	$H_2^+ + C_2H_6 \Rightarrow C_2H_3^+ + 2H_2 + H$	6.86E-16		[29]
R_{109}	$H_2^+ + C_2H_6 \Rightarrow C_2H_2^+ + 3H_2$	1.96E−16		[29]
R_{110}	$H_2^+ + C_2H_4 \Rightarrow C_2H_4^+ + H_2$	22.1E−16		[30]
R_{111}	$H_2^+ + C_2H_4 \Rightarrow C_2H_3^+ + H_2 + H$	18.1E−16		[30]
R_{112}	$H_2^+ + C_2H_4 \Rightarrow C_2H_2^+ + 2H_2$	8.8E-16		[29]
R_{113}	$H_2^+ + C_2H_2 \Rightarrow C_2H_2^+ + H_2$	48.2E−16		[29]
R_{114}	$H_2^+ + C_2H_2 \Rightarrow C_2H_3^+ + H$	4.8E−16		[29]
R_{115}	$H^+ + C_2H_6 \Rightarrow C_2H_4^+ + H_2 + H$	14E−16		[29]
R_{116}	$H^+ + C_2H_6 \Rightarrow C_2H_3^+ + 2H_2$	28E-16		[29]
R_{117}	$H^+ + C_2H_5 \Rightarrow C_2H_4^+ + H_2$	16.5E−16.		[29]
R_{118}	$H^+ + C_2H_5 \Rightarrow C_2H_3^+ + H_2 + H$	16.5E-16		[29]
R_{119}	$H^+ + C_2H_4 \Rightarrow C_2H_3^+ + H_2$	30E-16		[29]

II.6 Transport Coefficient:

The transport of charged and neutral species in the plasma is characterized by mobilities and diffusion coefficients, which must be specified in order to close the fluid equations.

II.6.1 Diffusion Coefficients for Neutral Species

The diffusion coefficient D_{ij} [$m^2\ s^{-1}$] of a neutral species j in a background gas i is calculated using the Chapman–Enskog equation [35]:

$$D_{ij} = \frac{3k_B T \sqrt{\frac{4\pi k_b T}{2m_{ij}}}}{16\, p\, \pi \sigma_{ij}^2\, \boldsymbol{\Omega_D}(\Psi)} \qquad \text{II-11}$$

where:

- k_B is the Boltzmann constant,
- T is the gas temperature,
- $m_{ij} = \frac{m_i m_j}{m_i + m_j}$ is the reduced mass of the two species,
- p is the gas pressure,
- $\sigma_{ij} = \frac{\sigma_i + \sigma_j}{2}$ is the collision diameter of species i and j,
- Ω_D is the collision integral for diffusion given by:

$$\Omega_D = \frac{A}{\Psi^B} + \frac{C}{e^{\Psi D}} + \frac{E}{e^{\Psi F}} + \frac{G}{e^{\Psi H}} \qquad \text{II-12}$$

Where A= 1.06036, B=0.15610, C= 0.19300, D= 0.47635, E=1.03587, F=1.52996, G= 1.76474, and H= 3.89411.

Ψ is the collision integral for diffusion, which depends on the dimensionless temperature.

$$\Psi = \frac{k_B T}{\epsilon_{ij}} \qquad \text{II-13}$$

With ε_{ij} *is the* binary temperature given by t $\varepsilon_{ij} = \sqrt{\varepsilon_i \varepsilon_j}$.

The Lennard–Jones parameters were calculated by linear interpolation

$$\sigma_{CH_x} = \sigma_{CH} + \frac{x-1}{3}(\sigma_{CH_4} - \sigma_{CH}) \quad \text{II-14}$$

where σ (m) and ϵ (J) represent the characteristic length and energy of each species in the Lennard–Jones potential. The values of these Lennard–Jones parameters have been reported for most neutral species by Reid et al. [36] and Svehla [37], while for the remaining species they were determined through linear interpolation.

Table II.6. Lennard–Jones Parameters and Polarizabilities of Species.

Species	σj (Å)	εj (K)	α (Å³)
CH_4	3.758	148.6	2.6
CH_3	3.620	121.6	
CH_2	3.491	95.2	
H	2.708	37.0	
C_2H_6	4.443	215.7	4.47
C_2H_3	4.443	215.7	
C_3H_8	5.115	237.1	6.33
CH	3.370	68.6	
H_2	2.827	59.7	0.819
C_2H_4	4.163	224.7	4.22
C_2H_2	4.033	231.8	3.49

The diffusion coefficient D_j of species j in the entire gas mixture, which accounts for the contributions of all background gases i, is determined from the individual D_{ij} values by applying Blanc's law [38].

$$\frac{p_{tot}}{D_j} = \sum_i \frac{p_i}{D_{ij}} \quad \text{II-15}$$

The ion mobility coefficient μ_{ij} of an ion j in a background gas i is calculated using Dalgarno's expression [39]:

$$\mu_{ij} = 0.514 \frac{T}{P_{tot}\sqrt{\alpha_i m_{ij}}} \quad \text{II-10}$$

With T denotes the background gas temperature (K), p the gas pressure (Pa), m_{ij} the reduced mass (amu), and α_i the polarizability $Å^3$ of the background gas, with the latter values taken from Böttcher and Bordewijk [40].

The ion diffusion coefficient D_j of an ion j is directly obtained using the Einstein relation, ensuring consistency with the physical approximations employed in the model [41].

$$D_j = \frac{k_b T_{ion}}{e} \mu_j \quad \text{II-11}$$

T_{ion} denotes the ion temperature, which is assumed to be equal to the gas temperature, and μ_j represents the mobility coefficient of the ion in the gas mixture.

II.7 Conclusion

In this chapter, we developed the theoretical and numerical framework for simulating dielectric barrier discharge in an Ar/CH_4 mixture. The plasma was modeled with a fluid approach, incorporating continuity equations for charged and neutral species, the drift–diffusion approximation, an electron energy balance, and Poisson's equation for the electric potential. Boundary and initial conditions accounted for surface charge accumulation on the dielectric and the applied sinusoidal voltage.

The reactor geometry and its implementation in COMSOL Multiphysics were presented, emphasizing solver choices and discretization strategies for stable solutions [42]. The plasma chemistry was described by identifying the main species and grouping reactions into electron-impact, ion–molecule, neutral–neutral, and recombination processes.

This framework provides a solid foundation for analyzing methane conversion and hydrogen production in the following chapters.

II.8 References:

[1] Fridman, A. (2008). *Plasma chemistry*. Cambridge University Press.

[2] Raizer, Y. P. (1991). *Gas discharge physics*. Springer.

[3] Lieberman, M. A., & Lichtenberg, A. J. (2005). *Principles of plasma discharges and materials processing* (2nd ed.). John Wiley & Sons.

[4] Chen, F. F. (2016). *Introduction to plasma physics and controlled fusion* (3rd ed.). Springer.

[5] Bogaerts, A., Neyts, E., Gijbels, R., & van der Mullen, J. (2002). Gas discharge plasmas and their applications. *Spectrochimica Acta Part B: Atomic Spectroscopy, 57*(4), 609–658.

[6] Pitchford, L. C., Alves, L. L., Bartschat, K., Biagi, S. F., Bordage, M. C., Bray, I., ... & Zatsarinny, O. (2017). LXCat: An open-access, web-based platform for data needed for modeling low temperature plasmas. *Plasma Processes and Polymers, 14*(1–2), 1600098.

[7] Sakai, O., & Tachibana, K. (2012). Modeling and numerical simulations of dielectric barrier discharges. *Plasma Sources Science and Technology, 21*(1), 013001.

[8] Eichwald, O., Ducasse, O., Merbahi, N., & Yousfi, M. (2011). Modeling and simulation of dielectric barrier discharges in air. *Plasma Sources Science and Technology, 20*(6), 065016.

[9] Kogelschatz, U. (2003). Dielectric-barrier discharges: Their history, discharge physics, and industrial applications. *Plasma Chemistry and Plasma Processing, 23*(1), 1–46.

[10] Hagelaar, G. J. M., & Pitchford, L. C. (2005). Solving the Boltzmann equation to obtain electron transport coefficients and rate coefficients for fluid models. *Plasma Sources Science and Technology, 14*(4), 722–733. https://doi.org/10.1088/0963-0252/14/4/011

[11] Y. M. A. Nedjar, M. Mostefaoui, and D. Benyoucef, “One-dimensional fluid modeling of methane dissociation in dielectric barrier discharge: Impact of voltage and dielectric constant,” PPT, vol. 12, no. 1, pp. 10–15, Aug. 2025, doi: 10.14311/ppt.2025.1.10.

[12] Donkó, Z. (2011). Particle simulations of low-pressure plasma sources. *Plasma Sources Science and Technology, 20*(2), 024001. https://doi.org/10.1088/0963-0252/20/2/024001

[13] Amine, N. Y. M., Mohamed, M., Djilali, B. (2025). Investigation of Ar/CH_4 Mixtures in Dielectric Barrier Discharge: A Simulation Approach for Hydrogen Production. Bulletin of Chemical Reaction Engineering & Catalysis, 20 (3), 458-470 (doi:10.9767/bcrec.20352).

[14] Fridman, A., & Kennedy, L. A. (2004). *Plasma physics and engineering*. Taylor & Francis.

[15] Capitelli, M., Ferreira, C. M., Gordiets, B. F., & Osipov, A. I. (2000). *Plasma kinetics in atmospheric gases*. Springer.

[16] Bittencourt, J. A. (2004). *Fundamentals of plasma physics* (3rd ed.). Springer.

[17] Shukla, P. K., & Mamun, A. A. (2002). *Introduction to dusty plasma physics*. Institute of Physics Publishing.

[18] Kolobov, V. I. (2006). Electron kinetics in microdischarges: Solving the Boltzmann equation in physical space. *Journal of Physics D: Applied Physics, 39*(3), R487–R506.

[19] Hagelaar, G. J. M., & Pitchford, L. C. (2005). BOLSIG+: Solving the Boltzmann equation. *Plasma Sources Science and Technology, 14*(4), 722–733.

[20] LXCat. (2023). The LXCat project: Electron scattering cross sections. Retrieved from https://nl.lxcat.net

[21] Capitelli, M., Celiberto, R., & Laricchiuta, A. (2016). Cross sections and rate coefficients for electron–molecule processes in plasma modeling. *Plasma Chemistry and Plasma Processing, 36*(1), 1–45.

[22] Gordiets, B. F., Ferreira, C. M., Guerra, V., & Loureiro, J. (1995). Kinetic model of a low-pressure N_2–O_2 flowing glow discharge. *Plasma Sources Science and Technology, 4*(3), 363–376.

[23] Choi, J. H., & Cho, M. (2001). Simulation of dielectric barrier discharges using fluid models. *IEEE Transactions on Plasma Science, 29*(4), 375–383.

[24] Gadoum, A., & Benyoucef, D. (2019). Set of the Electron Collision Cross Sections for Methane Molecule. IEEE Transactions on Plasma Science, 47(3), 1505–1513.

[25] Kosarev, I.N., Aleksandrov, N.L., Kindysheva, S.V., Starikovskaia, S.M., & Starikovskii, A. Yu. (2008). Kinetics of ignition of saturated hydrocarbons by nonequilibrium plasma: CH4-containing mixtures. Combustion and Flame, 154(3), 569–586.

[26] Gordillo-Vázquez, F.J., & Albella, J.M. (2004). Influence of the pressure and power on the non-equilibrium plasma chemistry of C2, C2H, C2H2, CH3and CH4affecting the synthesis of nanodiamond thin films from C2H2(1%)/H2/Ar-rich plasmas. Plasma Sources Science and Technology, 13(1), 50–57.

[27] Denysenko, I.B., Xu, S., Long, J.., Rutkevych, P.P., Azarenkov, N.A., & Ostrikov, K. (2004). Inductively coupled Ar/CH4/H2 plasmas for low-temperature deposition of ordered carbon nanostructures. Journal of Applied Physics, 95(5), 2713–2724.

[28] NISTchemical kinetics database. http://kinetcis.nist.gov/kinetics/

[29] The umist database for astrochemistry. http://udfa.ajmarkwick.net/index.php

[30] The kinetic database for astrochemistry. http://kida.astrochem-tools.org

[31] Mao, M., & Bogaerts, A. (2010). Investigating the plasma chemistry for the synthesis of carbon nanotubes/nanofibres in an inductively coupled plasma-enhanced CVD system: The effect of processing parameters. Journal of Physics D: Applied Physics, 43(31), 315203.

[32] Huntress, W.T., Jr. (1977). Laboratory studies of bimolecular reactions of positive ions in interstellar clouds, in comets, and in planetary atmospheres of reducing composition. The Astrophysical Journal Supplement Series, 33, 495.

[33] Jaritz, M., Hopmann, C., Behm, H., Kirchheim, D., Wilski, S., Grochla, D., Banko, L., Ludwig, A., Böke, M., Winter, J., Bahre, H., & Dahlmann, R. (2017). Influence of residual stress on the adhesion and surface morphology of PECVD-coated polypropylene.

[34] Baulch, D. L., Cobos, C. J., Cox, R. A., Esser, C., Frank, P., Just, T., ... & Troe, J. (1994). Evaluated kinetic data for combustion modeling. *Journal of Physical and Chemical Reference Data, 23*(6), 847–1033.

[35] Phelps, A. V. (1990). Cross sections and swarm parameters in noble gases and mixtures. *Journal of Physical and Chemical Reference Data, 19*(3), 653–675.

[36] Reid, R. C., Prausnitz, J. M., & Poling, B. E. (1987). *The properties of gases and liquids* (4th ed.). McGraw-Hill.

[37] Svehla, R. A. (1962). Estimated viscosities and thermal conductivities of gases using simplified Lennard–Jones potentials. NASA Technical Report R-132.

[38] Blanc, H. (1908). Diffusion of gases across a mixture. *Journal de Physique Théorique et Appliquée, 7*(1), 825–839.

[39] Böttcher, C. J. F., & Bordewijk, P. (1978). *Theory of electric polarization* (Vol. 2). Elsevier.

[40] Hagelaar, G. J. M., & Pitchford, L. C. (2005). Solving Boltzmann's equation for electrons in gases: BOLSIG+. *Plasma Sources Science and Technology, 14*(4), 722–733. https://doi.org/10.1088/0963-0252/14/4/011

[41] Alves, L. L. (2014). Electron energy distribution in low-temperature plasmas. *Plasma Sources Science and Technology, 23*(6), 063001.

[42] COMSOL Multiphysics®. (2023). *Plasma Module User's Guide*. COMSOL AB.

CHAPTER III: Plasma-Assisted Methane Conversion: Simulation Insights

III.1 Introduction

This chapter presents the numerical results of a dielectric barrier discharge (DBD) reactor operating in Ar/CH_4 mixtures. The analysis focuses on discharge characteristics and plasma chemistry, with particular emphasis on the effect of gas composition.

The model is first validated through comparison between simulated and experimental discharge current waveforms. Spatial distributions of charged and neutral species are then examined at peak current to characterize ionization and radical formation within the gap.

The temporal evolution of key species over one discharge cycle is analyzed to identify the dominant ionization and dissociation pathways. The influence of argon concentration is subsequently evaluated through its effect on discharge current, electron density, ion composition, radical formation, hydrogen production, and higher hydrocarbon suppression.

Finally, the results are interpreted in light of reported mechanisms to clarify the role of argon in enhancing methane conversion and hydrogen selectivity.

III.2 Model Validation

Before analyzing the effect of argon concentration, the simulation was first validated by comparing predicted discharge currents with experimental data from [1]. Figure III.1 shows the discharge current waveform for an Ar/CH_4 mixture (5% Ar, 95% CH_4).

The simulation reproduces the main features of the experimental waveform, including the peak amplitude and overall shape. The predicted peak current (0.097 mA) deviates by less than 3% from the measured value (0.10 mA). A small phase shift of about 4 μs is observed, which can be attributed to the numerical time resolution (0.5 μs) and to simplifications such as neglecting the external circuit response. Despite this shift, the agreement demonstrates that the model provides a reliable description of the discharge dynamics under atmospheric pressure.

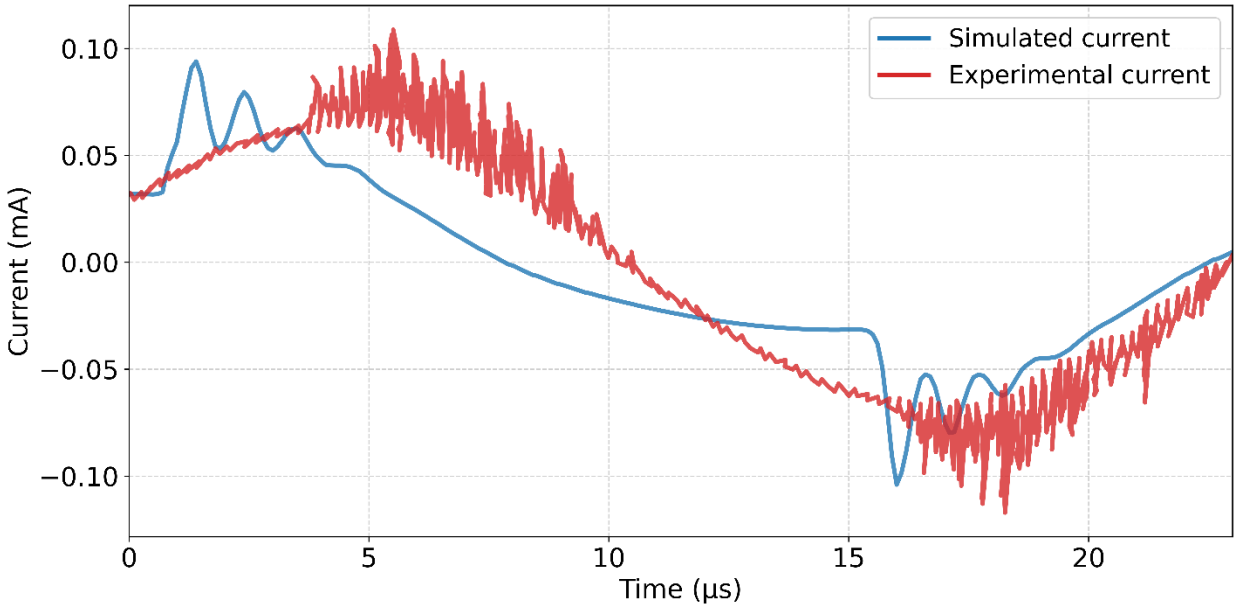

Figure III.1. Comparison between simulated and experimental discharge current profiles (Ar/CH_4, 5% Ar).

III.3 Spatial Distribution of Plasma Species

The spatial distribution of electrons, ions, and radicals across the discharge gap provides insight into how the plasma evolves during a discharge cycle. Figure III.2 and Figure III.3 presents the density profiles of major charged and neutral species at the instant of peak current (t = 30 μs).

The highest electron and ion densities are observed near the anode, where strong electric fields accelerate electrons and trigger ionization. The most abundant ions are CH_4^+, CH_3^+, CH_2^+, H^+, and H_2^+. Their production follows direct electron impact ionization of methane and subsequent ion–molecule reactions. The electron density decreases toward the cathode due to collisions and recombination processes.

On the neutral side, CH_3 is the dominant radical, produced mainly through dissociation of methane at a threshold of 8.8 eV. CH_2 and CH radicals appear later in the sequence, reflecting their higher excitation thresholds (≈ 9.4–12.5 eV). Hydrogen atoms (H) and molecules (H_2) are generated in significant amounts, highlighting the role of electron impact in sustaining methane cracking.

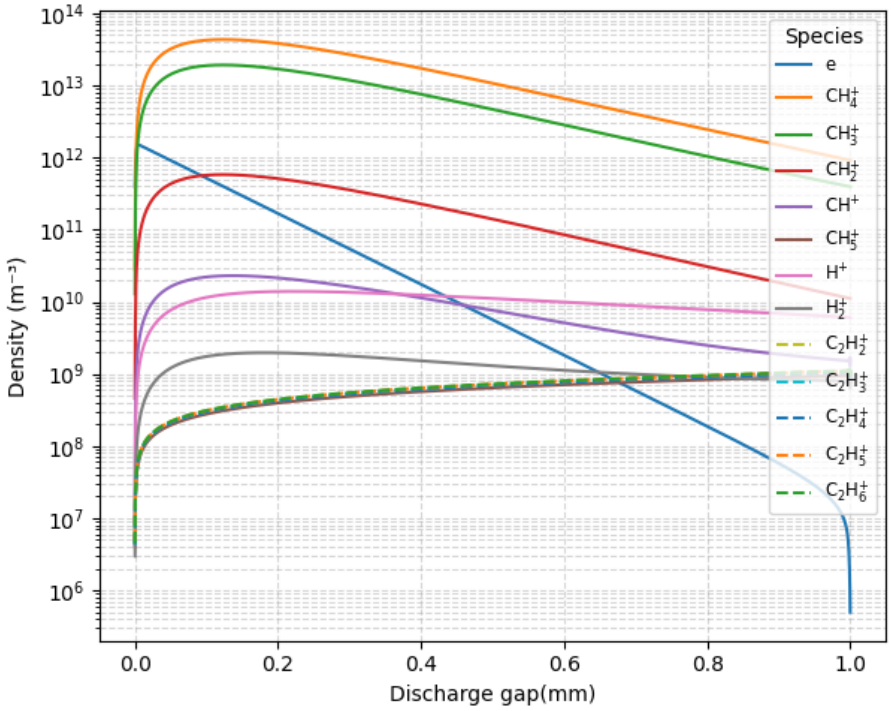

Figure III.2. Electron and Ion Profiles at Peak Discharge Current (t = 30 μs).

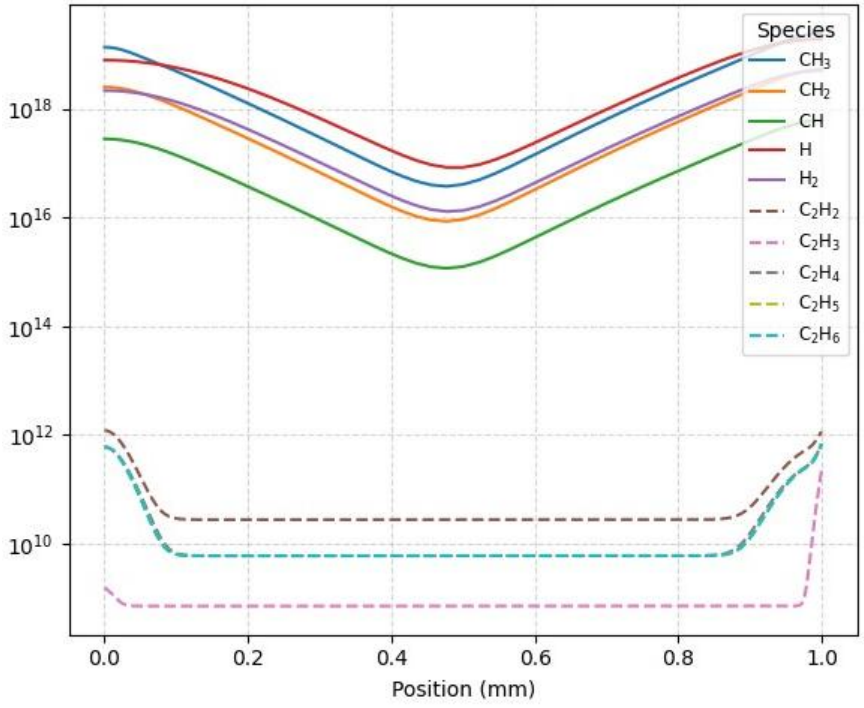

Figure III.3. Spatial Distribution of Radical Densities at Peak Discharge Current (t = 30 μs).

III.4 Temporal Evolution of Charged and Neutral Species

The time-dependent behavior of species densities reveals the link between discharge current and plasma chemistry. Figure III.4 and Figure III.5 shows the evolution of selected species densities over one discharge pulse, along with the current waveform.

The electron density rises sharply during the current peak due to strong ionization. Carbon-based ions (CH_3^+, CH_2^+, CH^+) appear almost simultaneously, while hydrogen-based ions (H_2^+, H^+) lag slightly because of their higher ionization potentials (15.4 eV for H_2, 13.6 eV for H). On the neutral side, CH_3 radicals are produced immediately after the current peak, followed by CH_2 and CH radicals. Hydrogen atoms and molecules accumulate more slowly, indicating that hydrogen formation is sustained throughout the discharge period.

This sequential formation pattern confirms that low-threshold electron processes dominate the early discharge phase, while high-threshold dissociation and recombination reactions govern the later phase.

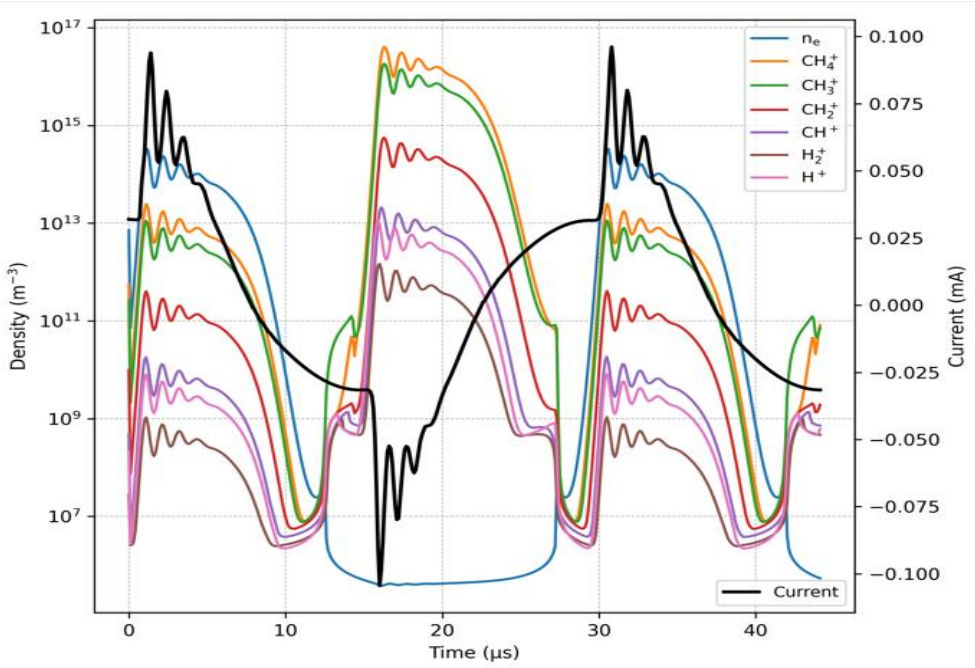

Figure III.4. Time Evolution of Electron and ion Densities and Discharge Current Waveform.

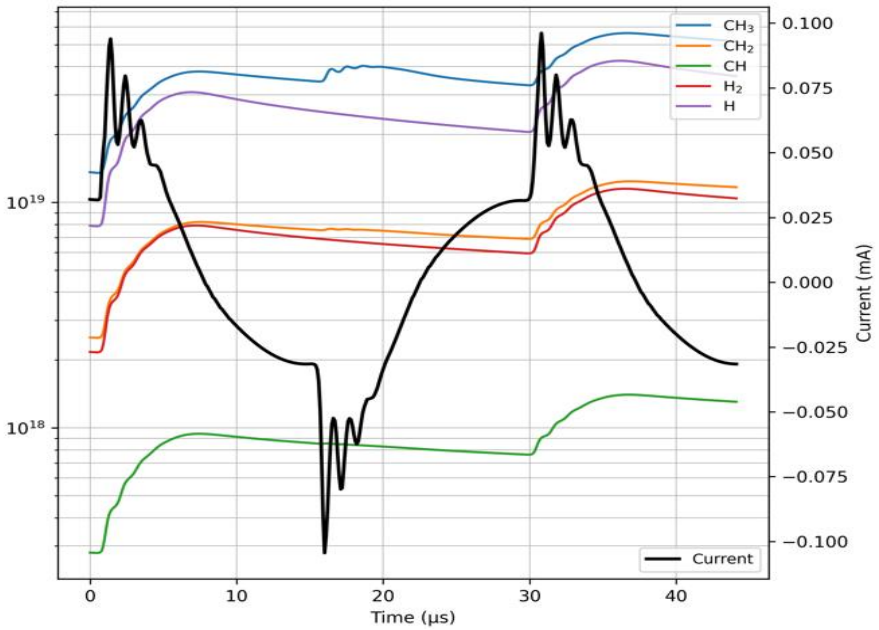

Figure III.5. Time Evolution of Radical Densities and Discharge Current Waveform.

III.5 Effect of Argon Concentration on Discharge Characteristics

To evaluate the influence of argon dilution, simulations were performed for Ar/CH_4 mixtures with argon concentrations ranging from 0% to 90%.

III.5.1 Discharge Current Behavior

Figure III.6 shows that the discharge current exhibits one peak per half-cycle for all mixtures. As the argon fraction increases, the peak current also increases. The maximum current (0.12 A) occurs at 80% Ar. This enhancement results from argon's high ionization potential, which facilitates electron multiplication and early ignition of microdischarges. At 90% Ar, the peak current decreases slightly due to the reduced methane fraction, which limits the availability of molecules for ionization and dissociation.

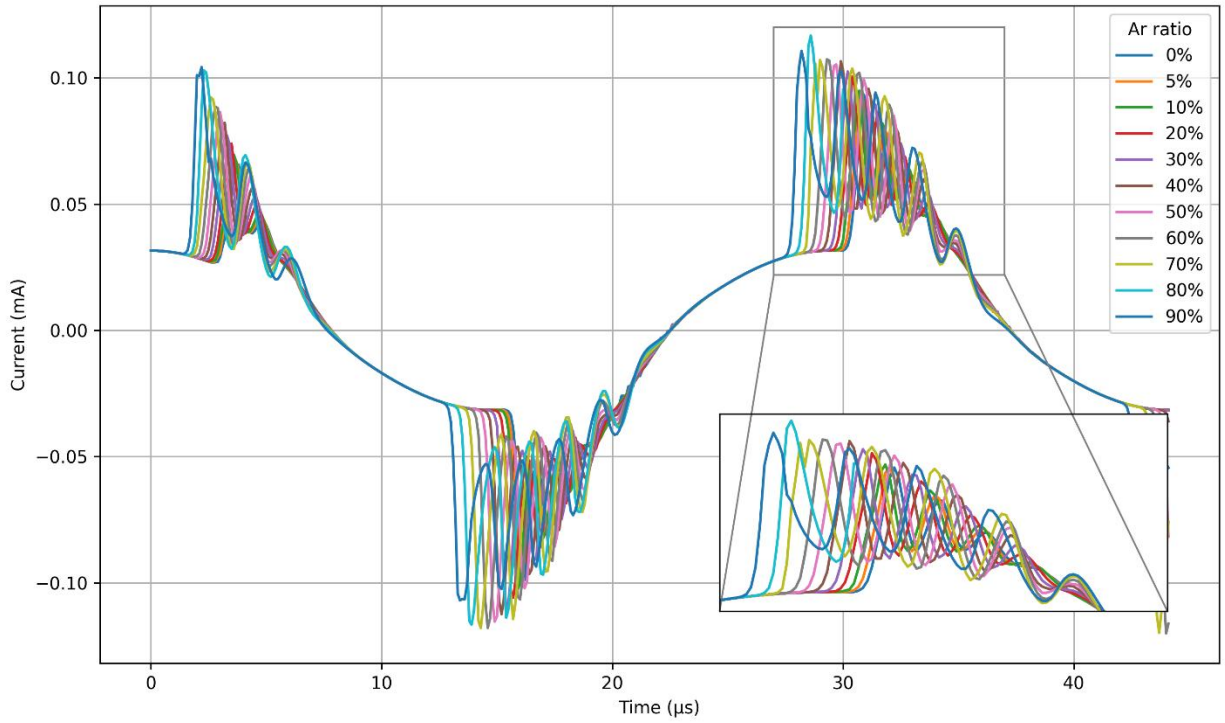

Figure III.6. Discharge Current Waveform at Different Ar/CH_4 Ratios.

III.5.2 Electron Density Profiles

Figure III.7 presents the electron density distribution across the discharge gap at t = 29.8 μs for different Ar/CH_4 mixtures. Increasing the argon fraction leads to higher electron densities, particularly near the anode where the electric field is strongest. The maximum density, approximately 10^{15} m^{-3}, is obtained at 90% Ar. The 80% Ar case shows a slightly lower value at this instant because the discharge current is already decreasing, whereas other mixtures remain in their rising phase. This behavior reflects the transient nature of filamentary discharges.

The overall increase in electron density and discharge current with argon addition is consistent with previous studies. Jo et al. [2] reported that argon enhances the population of high-energy electrons through stepwise ionization and metastable states (Ar*), thereby strengthening electron-impact processes. Our simulations confirm this mechanism, showing nearly an order-of-magnitude rise in electron density when the argon fraction increases from 0% to 80%.

Furthermore, De Bie et al. [3] demonstrated that noble-gas dilution stabilizes the discharge and improves plasma uniformity. The smooth increase in current amplitude observed in our results supports this stabilizing effect. However, excessive argon dilution reduces methane availability, which explains the decline in radical and hydrogen densities at high Ar fractions.

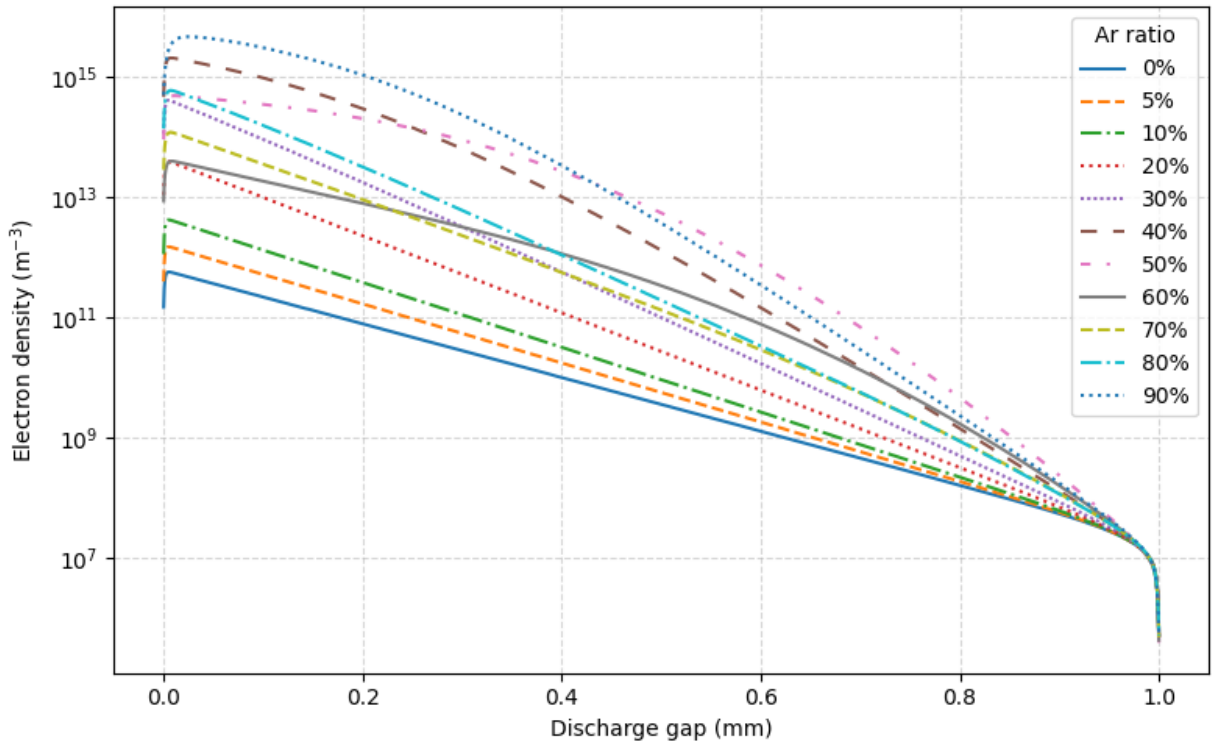

Figure III.7. Spatial electron density distribution for different Ar/CH_4 mixtures.

III.6 Influence of Argon on Plasma Chemistry

III.6.1 Ion Species Evolution

Figure III.8 shows the variation of ion species densities with argon concentration. At low argon levels (0–40%), methane-derived ions (CH_3^+, CH_2^+, CH^+) dominate. As argon fraction increases above 70%, Ar^+ becomes the major ion, indicating a shift in ionization dynamics. The rise in electron density with argon confirms its role in sustaining ionization while reducing energy losses in inelastic collisions.

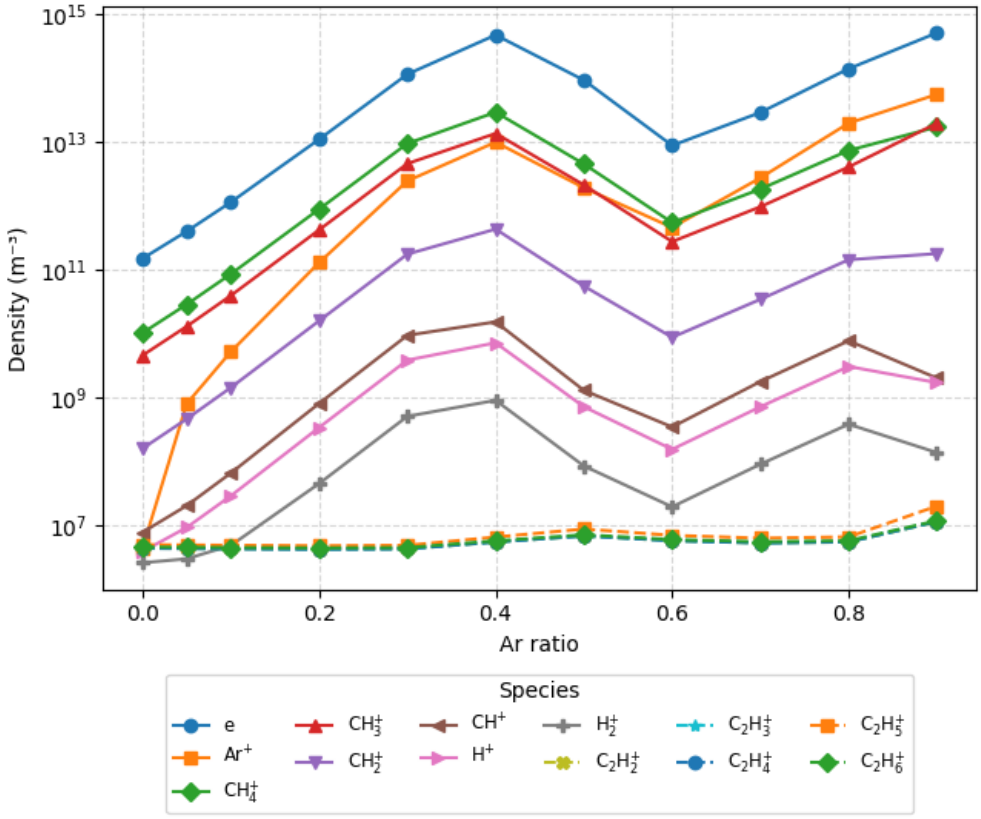

Figure III.8. variation of ion And Electron densities with argon concentration.

III.6.2 Radical and Hydrogen Production

Figure III.9 illustrates the variation of key radicals and hydrogen densities as a function of argon concentration. The methyl radical (CH_3) is the dominant methane fragment and exhibits the largest increase, rising from 1.3×10^{19} m^{-3} to 1.7×10^{19} m^{-3} at approximately 50% Ar. CH_2 and CH follow similar trends but with lower densities. Hydrogen atoms and molecules also increase with argon addition, reaching a maximum H_2 density of 3.1×10^{18} m^{-3} near the 50:50 Ar/CH_4 ratio. Beyond this composition, both radical and hydrogen densities decline due to methane dilution, which limits further dissociation.

The dominance of CH_3 agrees with theoretical and experimental studies showing that electron-impact dissociation of CH_4 primarily produces methyl radicals under typical DBD conditions [4][5]. PF-LIF measurements in atmospheric-pressure Ar/CH_4 discharges further confirm CH_3 as the principal radical species [6]. The observed increase in radical and hydrogen densities at

intermediate argon fractions results from enhanced electron density and higher-energy electron populations promoted by argon metastables and stepwise ionization processes. However, at high argon fractions (>≈70%), the reduced methane partial pressure becomes the limiting factor, leading to decreased methane conversion and hydrogen production. This behavior is consistent with trends reported in previous experimental studies [2][3], which also identified intermediate noble-gas dilution as optimal for maximizing hydrogen yield.

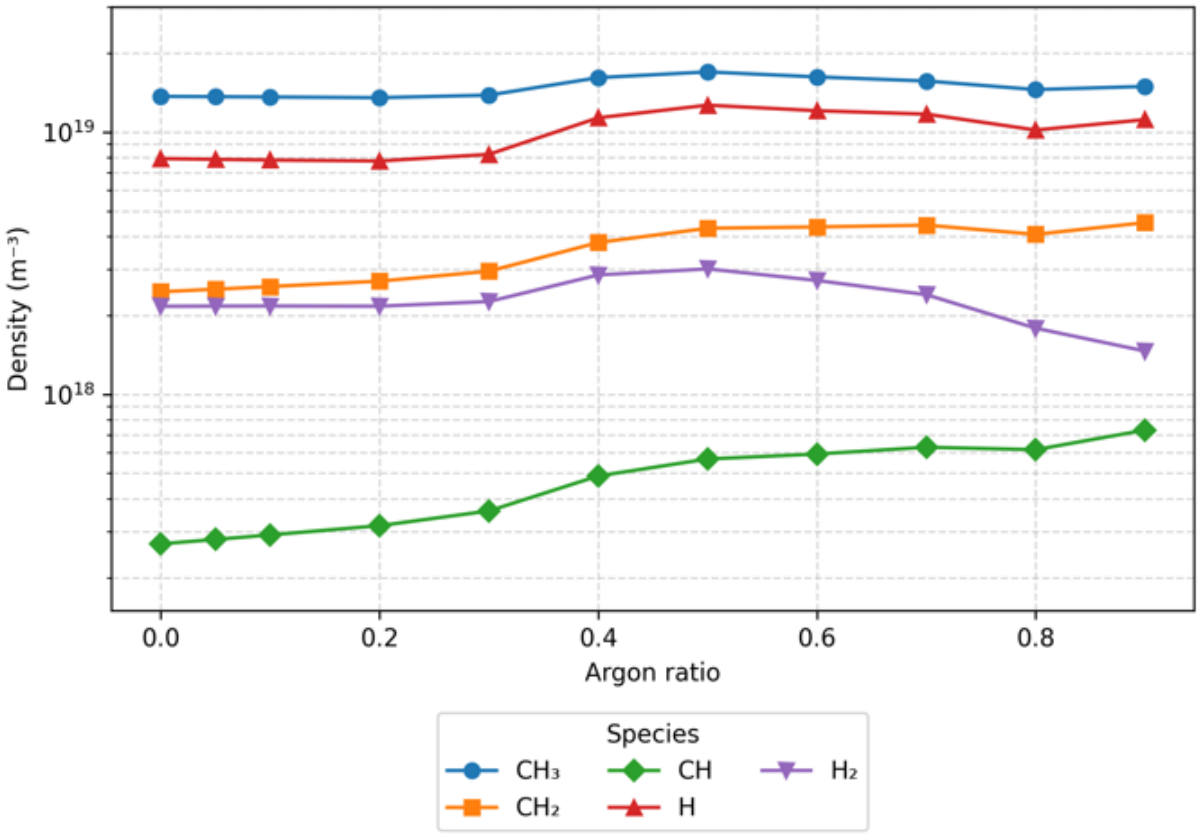

Figure III.9. Effect of Argon Radical formation.

III.6.3 Higher Hydrocarbons

Stable hydrocarbons such as C_2H_2, C_2H_4, and C_2H_6 decrease as the argon fraction increases (Figure III.10). These species are primarily formed through secondary pathways, including ion–neutral, radical–radical, and three-body reactions, which compete with direct electron-impact dissociation. As argon concentration rises, the discharge favors fragmentation mechanisms that generate H atoms and small radicals rather than recombination routes leading to heavier

hydrocarbons. This shift explains the suppression of C_2 species in argon-rich plasmas and is consistent with experimental observations reported in the literature [1][3].

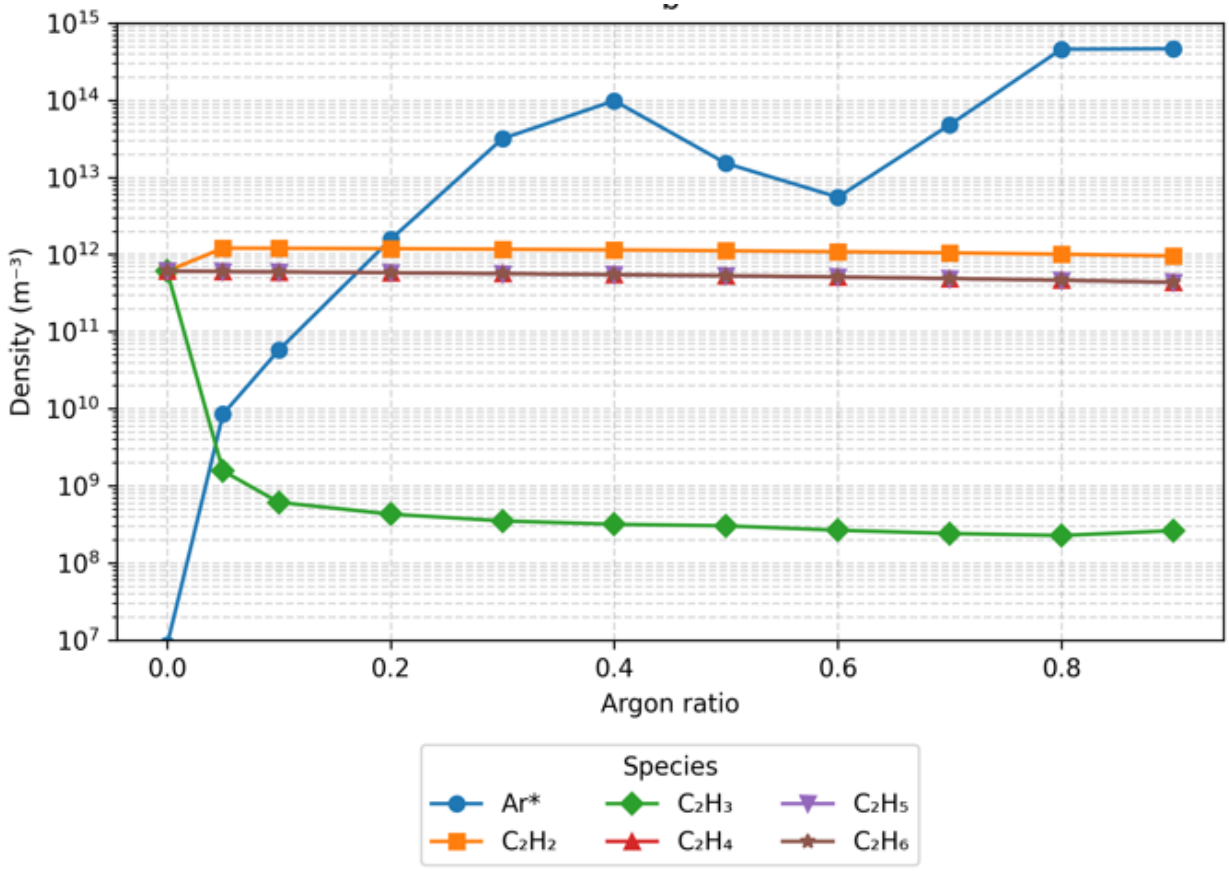

Figure III.10. Effect of Ar/CH_4 ratio on higher hydrocarbon production.

III.7 Conclusion

This chapter investigated the influence of argon dilution on methane conversion in a dielectric barrier discharge reactor. Model validation showed excellent agreement with experimental current waveforms, with less than 3% deviation in peak amplitude, confirming the reliability of the numerical framework.

The results demonstrate that increasing the argon fraction enhances electron density and discharge intensity through improved ionization dynamics. This promotes methane fragmentation and leads to dominant CH_3 radical formation, which subsequently contributes to hydrogen generation through further dissociation and hydrogen abstraction reactions.

Hydrogen production increases with argon addition up to an optimal composition of approximately 50:50 Ar/CH_4, where enhanced electron-impact dissociation is balanced by sufficient methane availability. At higher argon fractions, methane dilution becomes the limiting factor, reducing radical densities and hydrogen yield while suppressing the formation of heavier hydrocarbons (C_2 species).

These findings confirm that careful optimization of the Ar/CH_4 ratio is essential to maximize hydrogen selectivity and overall reactor performance.

III.8 Reference

[1]. Barni, R., & Riccardi, C. (2018). Gas-phase evolution of Ar/H2O and Ar/CH4 dielectric barrier discharge plasmas. The European Physical Journal D, 72(4), 62.

[2]. Jo, S., Hoon Lee, D., Seok Kang, W., & Song, Y.-H. (2013). Methane activation using noble gases in a dielectric barrier discharge reactor. Physics of Plasmas, 20(8), 083509.

[3]. De Bie, C., van Dijk, J., & Bogaerts, A. (2015). The Dominant Pathways for the Conversion of Methane into Oxygenates and Syngas in an Atmospheric Pressure Dielectric Barrier Discharge. The Journal of Physical Chemistry C, 119(39), 22331–22350.

[4]. Ziółkowski, M., Vikár, A., Mayes, M. L., Bencsura, Á., Lendvay, G., & Schatz, G. C. (2012). *Modeling the electron-impact dissociation of methane.* Journal of Chemical Physics, 137(22), 22A510.

[5]. Erwin, D. A., & Kunc, J. A. (2005). *Electron-impact dissociation of the methane molecule into neutral fragments.* Physical Review A, 72(5), 052719.

[6]. Nilsson, S., Ravelid, J., Park, J., Cha, M. S., & Ehn, A. (2024). *Photofragmentation laser-induced fluorescence imaging of CH_3 by structured illumination in a plasma discharge.* Optics Express, 32(15), 26492–26499.

Chapter IV: Solid Oxide Fuel Cells: Performance and Fuel Utilization

IV.1 Introduction

Solid oxide fuel cells (SOFCs) have attracted considerable attention due to their high efficiency, fuel flexibility, and potential for integration with renewable energy systems [1,2]. Hydrogen is often used as the reference fuel because of its straightforward electrochemical oxidation and lack of carbon deposition issues [3]. In practical applications, however, SOFCs frequently operate with alternative fuels such as methane or ammonia, which require internal reforming or decomposition for effective electrochemical utilization [4–7].

In this chapter, a detailed Multiphysics model is employed to analyze the performance of anode-supported SOFCs under various fuel conditions. The results are presented through polarization and power density curves, mole fraction distributions, and electrolyte current density profiles. The analysis begins with hydrogen operation under different stoichiometry factors (λ = 1, 3, and 5), then explores performance with methane–hydrogen mixtures, and concludes with an evaluation of ammonia as a carbon-free fuel candidate.

IV.2 Modeling

IV.2.1 Physical structure of the SOFC unit cell

The modeled configuration is a planar anode-supported SOFC consisting of a porous anode substrate, a thin electrolyte, and a porous cathode. Gas channels supply the fuel (H_2, NH_3, or CH_4 mixtures) on the anode side and air on the cathode side. The electrochemical reactions are:

- **Anode (fuel oxidation):**

$$H_2 + O^{2-} \rightarrow H_2O + 2e^-$$

- **Cathode (oxygen reduction):**

$$\frac{1}{2}O_2 + 2e^- \rightarrow O^{2-}$$

- **Overall cell reaction:**

$$H_2 + \frac{1}{2}O_2 \rightarrow H_2O + \text{heat} + \text{electric power}$$

For ammonia-fueled operation, thermal or catalytic decomposition upstream converts NH_3 into H_2 and N_2, which are then electrochemically consumed. Similarly, when methane or biogas is used, reforming and water–gas shift reactions must be considered.

IV.2.2 Governing equation

IV.2.2.1 Charge Conservation

The electronic and ionic charge transport in the electrodes and electrolyte are described by Ohm's law, ensuring that current is conserved within each conducting domain [9,10].

- **For the Ionic phase:**

$$\nabla .\ i_i = Q_l \qquad i_l = -\sigma_l \nabla \varphi_l$$

- **For the Electronic phase:**

$$\nabla . i_s = Q_s \qquad i_s = -\sigma_s \nabla \varphi_s$$

where i_l i_s are ionic and electronic current densities, σ_l and σ_s are conductivities, and φ_l, φ_s the electric potentials.

IV.2.2.2 Charge balances

Charge balance is enforced in the electrodes, electrolyte, and current feeders through the Secondary Current Distribution interface**,** with the charge transfer current density at the electrode–electrolyte interfaces described by Butler–Volmer kinetics [8,11].

IV.2.2.3 Anode Kinetics

At the anode, hydrogen is oxidized to form water. Assuming that the first electron transfer is the rate-determining step, the charge transfer current density is given by:

$$i_{a,ct} = i_{0,a}\left[\frac{c_{h2}}{c_{h2ref}}\exp\left(\frac{0.5F}{RT}\eta\right) - \frac{c_{h2o}}{c_{h2oref}}\exp\left(\frac{-1.5F}{RT}\eta\right)\right] \quad \text{IV-1}$$

$i_{0,a}$ = Anode exchange current density (A/m2), C_{h2} = Molar concentration of hydrogen,

C_{h2o} = Molar concentration of water, C_t = Total concentration of species (mol/m3),

$C_{h2,\,ref}$ = Reference concentrations (mol/m3), $C_{h2o,\,ref}$ = Reference concentrations (mol/m3),

F = Faraday's constant (C/mol), R = gas constant (J/(mol·K)

T = temperature (K) η = overvoltage (V) For the cathode, use the Relation

IV.2.2.4 Cathode Kinetics

At the cathode, oxygen reduction is described by:

$$i_{c,ct} = i_{0c}\left[\exp\left(\frac{3.5F}{RT}\eta\right) - x_{o2}\frac{c_t}{c_{o2ref}}\exp\left(\frac{-0.5F}{RT}\eta\right)\right] \quad \text{IV-2}$$

With $i_{0,c}$= Cathode exchange current density (A/m2), and X_{o2}= Molar fraction of oxygen

IV.2.2.5 Overpotential Definition

The local overpotential is defined as:

$$\eta = \varphi_{electronic} - \varphi_{ionic} - \Delta\varphi_{eq} \quad \text{IV-3}$$

Where $\Delta\varphi_{eq}$ is the equilibrium potential difference (V), obtained from the Nernst relation [3].

IV.2.2.6 Cell Voltage

To set up the above charge transfer expressions. the Concentration Dependent Kinetics expression type is used. The potential is fixed to reference potential zero at the anode's inlet boundary, set the potential to the cell voltage, V_{cell} at the cathode's inlet boundary. The rest is explained in the following

The overall cell voltage is expressed as:

$$V_{cell} = \Delta\varphi_c - \Delta\varphi_a - V_{pol} \qquad \text{IV-4}$$

With V_{pol} = polarization $\Delta\varphi_a = 0V$ $\Delta\varphi_c = 1V$

Where V_{pol} is the polarization loss, $\Delta\varphi_a$ is the anode potential (set to 0 V at the inlet), and $\Delta\varphi_c$ is the cathode potential (set to the applied cell voltage). This definition links the electrode potentials with the externally applied voltage, consistent with SOFC modeling frameworks [9].

IV.2.3 Characteristic of SOFC fuel cell:

IV.2.3.1 Description of geometry:

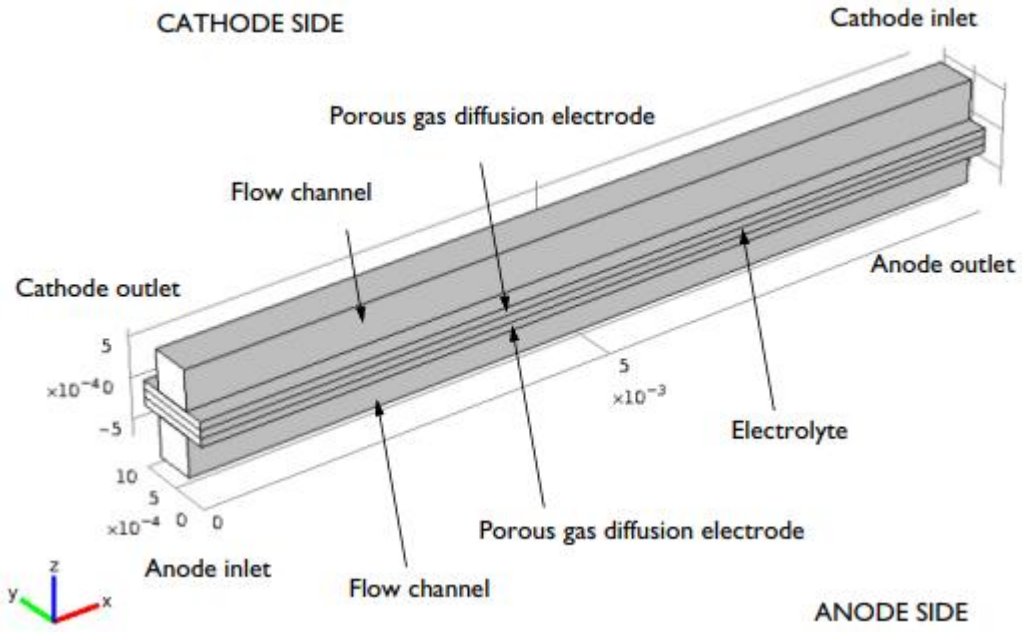

Figure IV.1. geometry of SOFC Fuel cell.

IV.2.3.2 Model parameter

Table IV.1. Model Parameters for the Solid Oxide Fuel Cell Simulation.

Parameters	Value
Electrolyte Thickness	1.5×10^{-4} [m]
Electrode Thickness	2×10^{-4} [m]

Gas flow channel height and width each	0.5×10^{-3} [m]
Gas flow channel length	5×10^{-3} [m]
Porosity	0.3 (30%)
Reference diffusivity	3.16×10^{-8} [m²/s]
Electrolyte conductivity	10 [S/m]
Electrodes conductivity	1000 [S/m]
Cathode voltage	1 [V]
Anode voltage	0 [V]
Electrodes permeability	1×10^{-10} [m²]
Specific surface area of each electrode	1×10^{9} [1/m]
Exchange current density at cathode	0.01 [A/m²]
Exchange current density at anode	0.1 [A/m²]
Viscosity of air	3×10^{-5} [Pa*s]
Atmospheric pressure	1 [atm]
Temperature	800 [°C]

IV.3 Result and discussion

IV.3.1 Effect of Stoichiometry (λ) on SOFC Performance

In this section, the performance of the SOFC unit cell under different fuel stoichiometry factors (λ) is presented and discussed. The results include polarization characteristics, power density curves, and species concentration distributions. These outputs provide insights into the dominant loss mechanisms and fuel utilization under varying operating conditions.

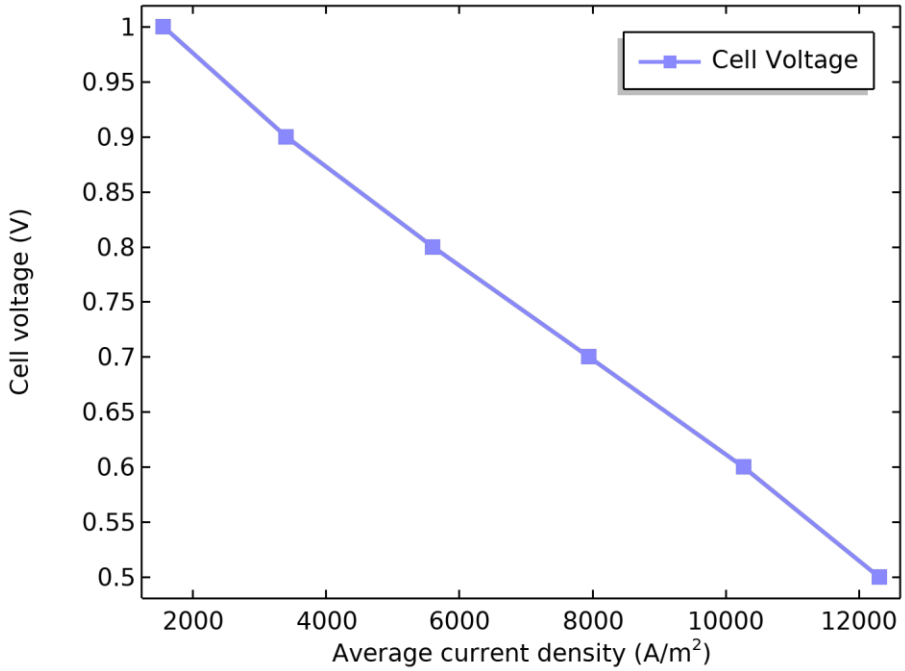

Figure IV.2. Polarization and power density curves of the SOFC at λ = 1 (stoichiometric hydrogen feed).

The polarization curve for λ = 1 exhibits the characteristic three regions of cell operation. Activation losses are nearly absent in the model. This reflects the assumption of rapid electrode kinetics in COMSOL Multiphysics. Experimentally, this region is more pronounced due to slower reaction rates. The intermediate portion of the curve is almost linear, indicating that ohmic losses dominate. These losses originate from the finite ionic conductivity of the electrolyte and constitute the main contribution to the voltage drop. At higher current densities, the curve declines sharply. This decline is associated with concentration (mass transport) losses. Under stoichiometric conditions (λ = 1), this effect is amplified. Complete hydrogen consumption near the anode outlet leads to fuel depletion and significant mass transport limitations.

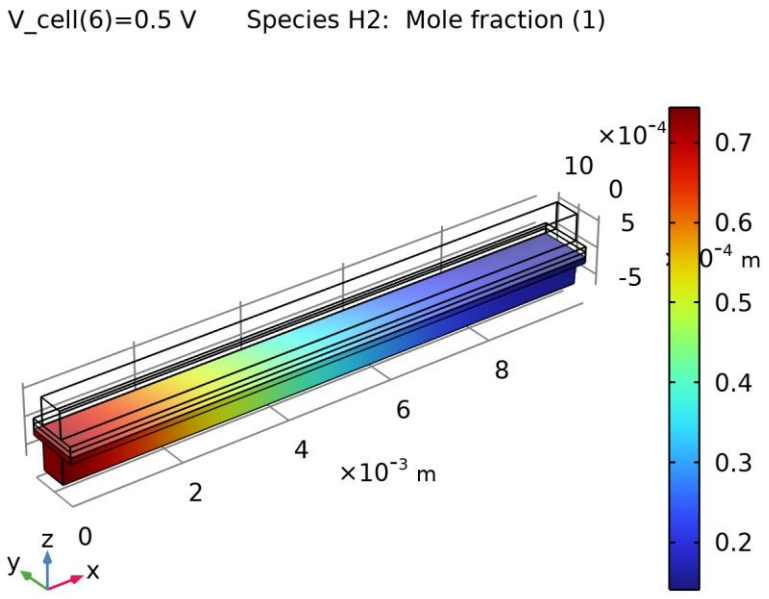

Figure IV.3. Hydrogen mole fraction distribution in the anode gas channel at λ = 1 and 0.5 V.

At stoichiometric conditions (λ = 1), hydrogen is nearly completely consumed along the anode channel (Figure IV.3). Its mole fraction drops sharply from the inlet to the outlet. Near the outlet, hydrogen depletion becomes severe. This depletion explains the strong concentration polarization in the polarization curve, as insufficient hydrogen reaches the electrochemically active sites.

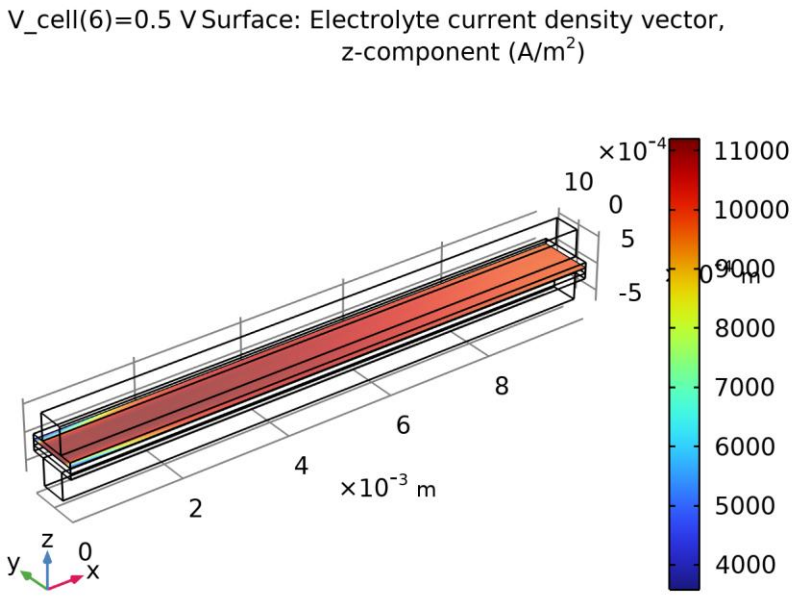

Figure IV.4. Current Density Distribution in the Electrolyte (λ = 1, V = 0.5).

The current density distribution at stoichiometric conditions (λ = 1) is highly non-uniform. The highest current occurs near the anode inlet, where hydrogen concentration is greatest (Figure IV.4). Toward the outlet, the current drops sharply due to fuel depletion. This uneven distribution explains the rapid onset of concentration polarization in the polarization curve (Figure IV.1).

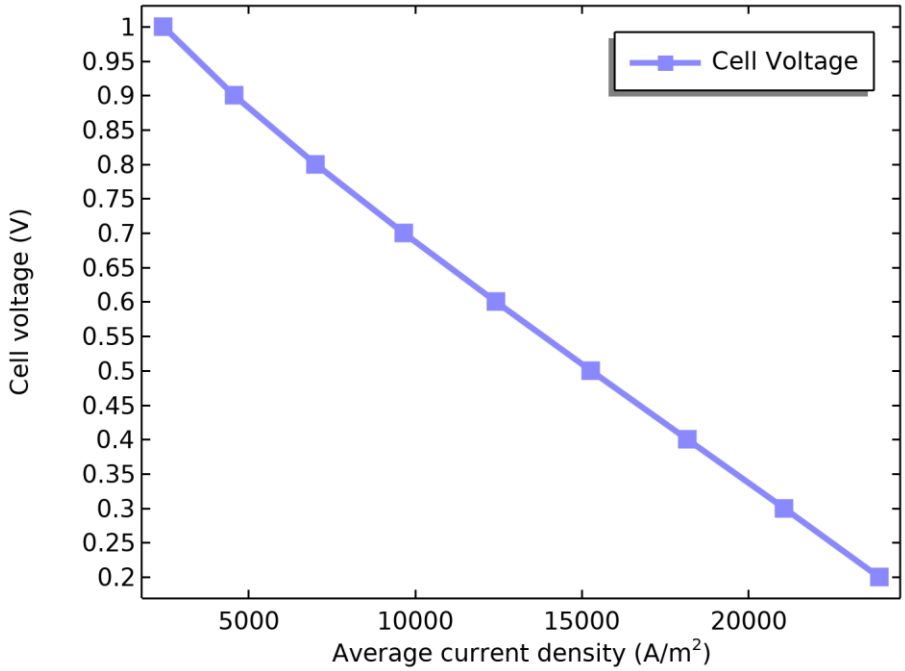

Figure IV.5. Polarization and power density curves of the SOFC at λ = 3 (moderate hydrogen excess).

The polarization curve for λ = 3 shows improved stability compared to the stoichiometric case. At 0.7 V, the cell reaches a current density of approximately 9.6×10^3 A·m^{-2} (0.96 A·cm^{-2}). The maximum power density is about 7.4×10^3 W·m^{-2} (0.74 W·cm^{-2}) at 0.6 V. The activation region remains negligible, while the ohmic region dominates most of the curve, showing a nearly linear voltage drop. Mass transport limitations appear only at very high current densities. They are less pronounced than in the λ = 1 case due to the higher hydrogen excess. This confirms that increasing λ reduces fuel starvation and improves performance uniformity, though overall fuel utilization decreases.

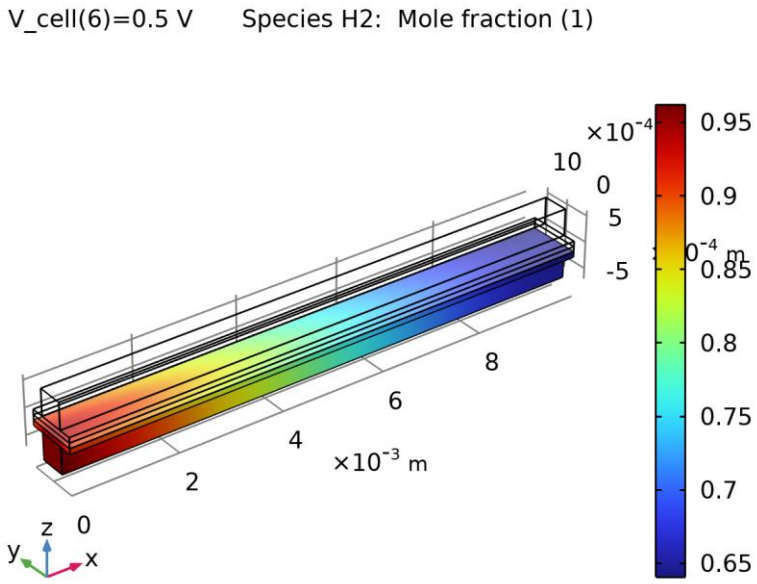

Figure IV.6. Hydrogen mole fraction distribution in the anode gas channel at λ = 3 and 0.5V.

With moderate excess fuel (λ = 3), the hydrogen mole fraction profile shows a smoother gradient across the channel length (Figure IV.6). Hydrogen remains available even at the outlet, which reduces mass transport limitations compared with λ = 1. This leads to higher achievable current densities and delays the onset of concentration polarization. The more uniform distribution also indicates improved current sharing along the electrode, which contributes to better cell stability and durability.

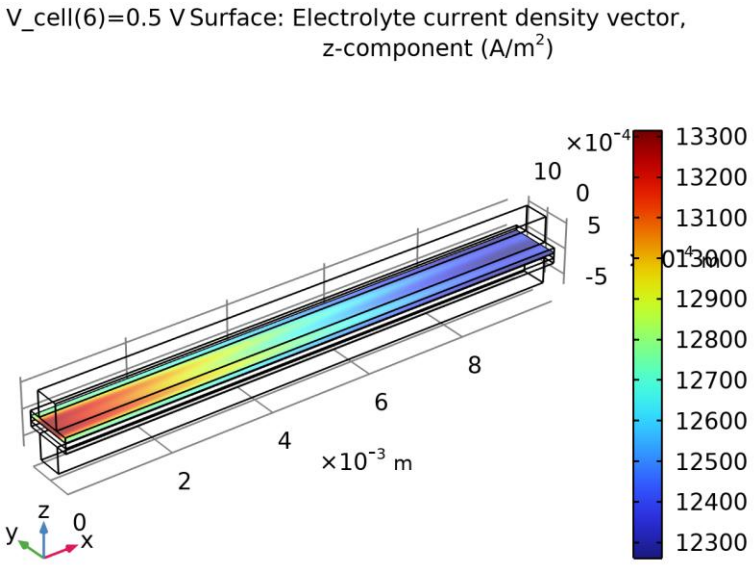

Figure IV.7. Current Density Distribution in the Electrolyte (λ = 3, V = 0.5).

The electrolyte current density (Figure IV.7) is more uniform compared with λ = 1. Higher hydrogen availability sustains significant current along the entire channel, reducing the inlet–outlet gradient. This improvement aligns with the polarization curve (Figure IV.5), where higher current densities are reached before concentration losses appear.

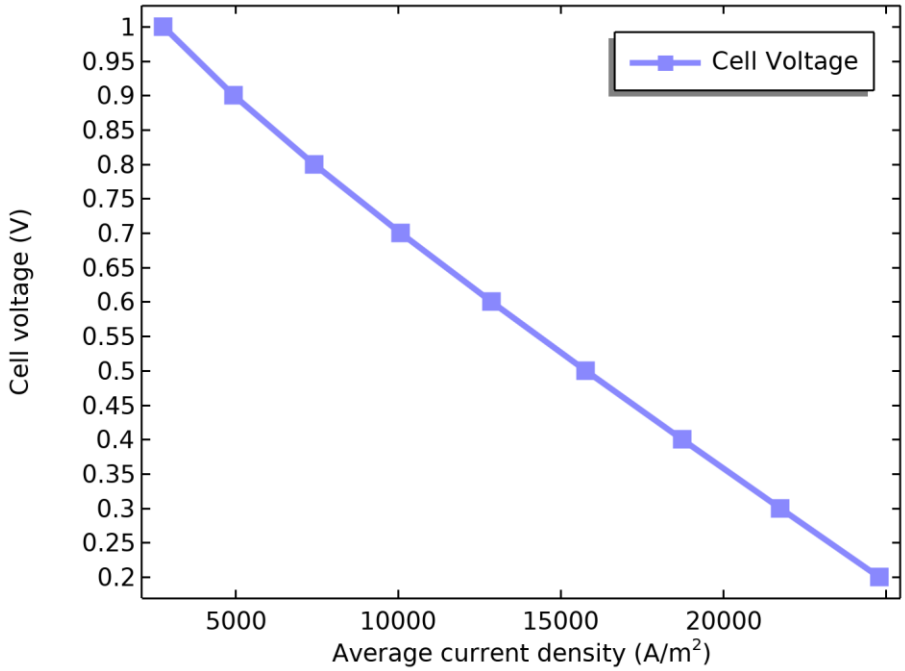

Figure IV.8. Polarization and power density curves of the SOFC at λ = 5 (high hydrogen excess).

The polarization curve for λ = 5 (Figure IV.8) illustrates the effect of a large hydrogen excess. At 0.7 V, the current density reaches 1.0×10^4 A·m^{-2} (1.01 A·cm^{-2}), higher than for both λ = 1 and λ = 3. The maximum power density occurs at 0.6 V, with a value of about 7.7×10^3 W·m^{-2} (0.77 W·cm^{-2}). Compared with lower stoichiometries, the curve remains linear over a wider current range. Activation losses are negligible, and ohmic resistance continues to dominate. Mass transport limitations appear only at very high current densities (below 0.4 V), showing that the larger fuel excess effectively prevents fuel starvation. However, this performance gain comes at the expense of fuel utilization, as only about 20% of the supplied hydrogen is electrochemically consumed at λ = 5.

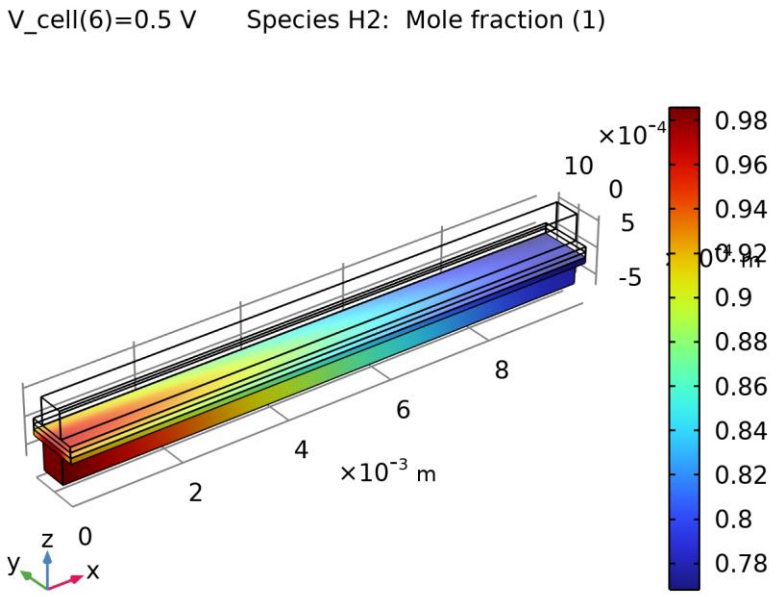

Figure IV.9. Hydrogen mole fraction distribution in the anode gas channel at λ = 5 and 0.5 V.

At high fuel excess (λ = 5), the hydrogen mole fraction remains nearly constant along the anode channel (Figure IV.9). Very little depletion occurs, indicating that fuel starvation is almost completely avoided. This explains the extended linear region of the polarization curve and the highest current density among all stoichiometries. However, a large fraction of hydrogen exits unreacted, reducing overall fuel utilization efficiency.

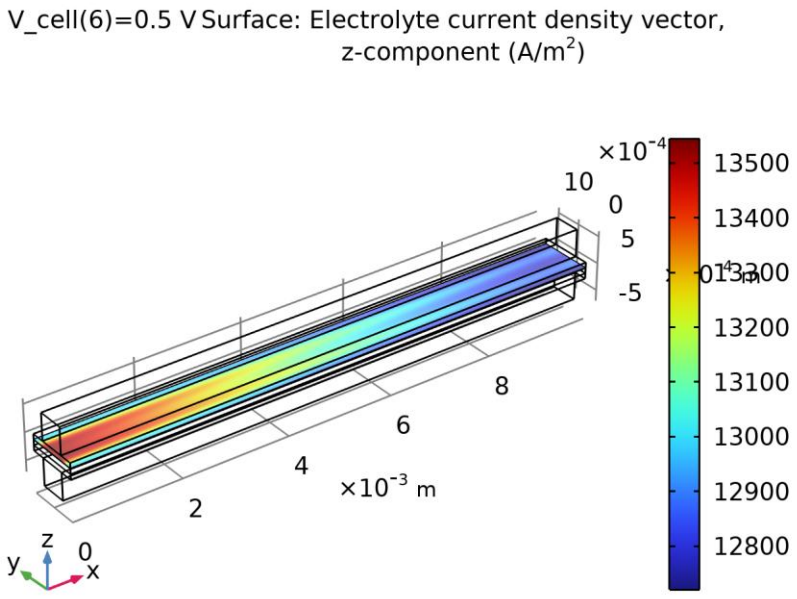

Figure IV.10. Electrolyte current density at λ = 5 and 0.5 V.

The electrolyte current density distribution is nearly flat, indicating uniform current generation across the channel. This matches the polarization behavior in Figure IV.8, where ohmic losses dominate and concentration polarization appears only at very high current densities.

IV.3.2 SOFC Performance with Methane–Hydrogen Mixtures:

Methane is one of the most abundant and widely used hydrocarbon fuels. Its use in SOFCs is attractive due to availability and low cost. However, methane cannot be directly oxidized electrochemically at the anode. It therefore requires internal or external reforming to produce hydrogen. To investigate methane-rich fuels, the model was applied to a CH_4/H_2 (70/30) mixture. The resulting performance and species distributions were analyzed.

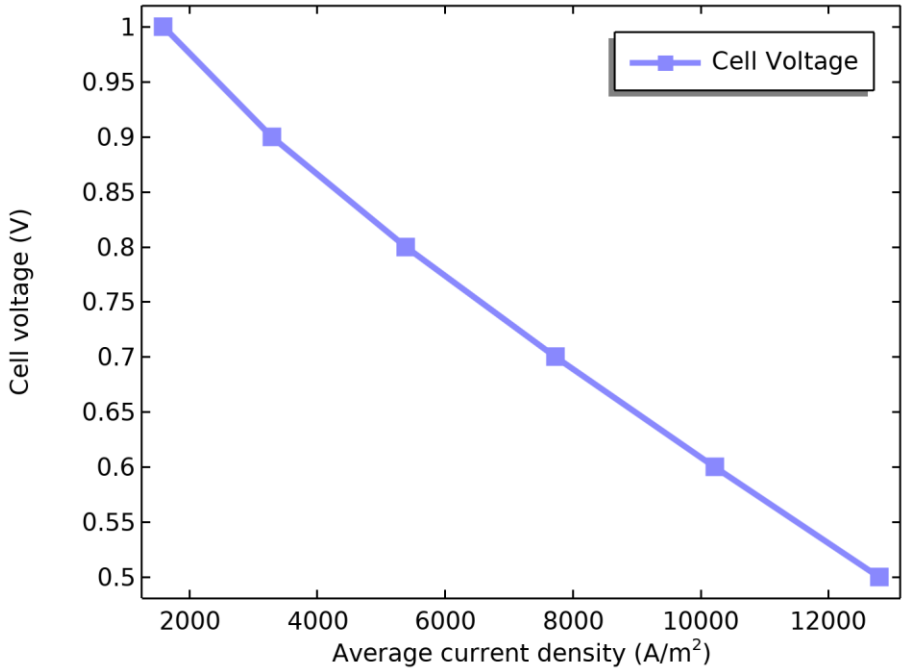

Figure IV.11. Polarization and power density curves of the SOFC for CH_4/H_2 Gas mixture.

When operating on a CH_4/H_2 (70/30) mixture, the polarization curve shows lower current density compared with pure hydrogen (Figures IV.2, IV.5, IV.8). The maximum power density is also reduced. This behavior corresponds to the mole fraction distributions (Figures IV.13, IV.14). Hydrogen decreases significantly along the anode channel, while methane remains nearly constant because it is not directly electrochemically oxidized in the model.

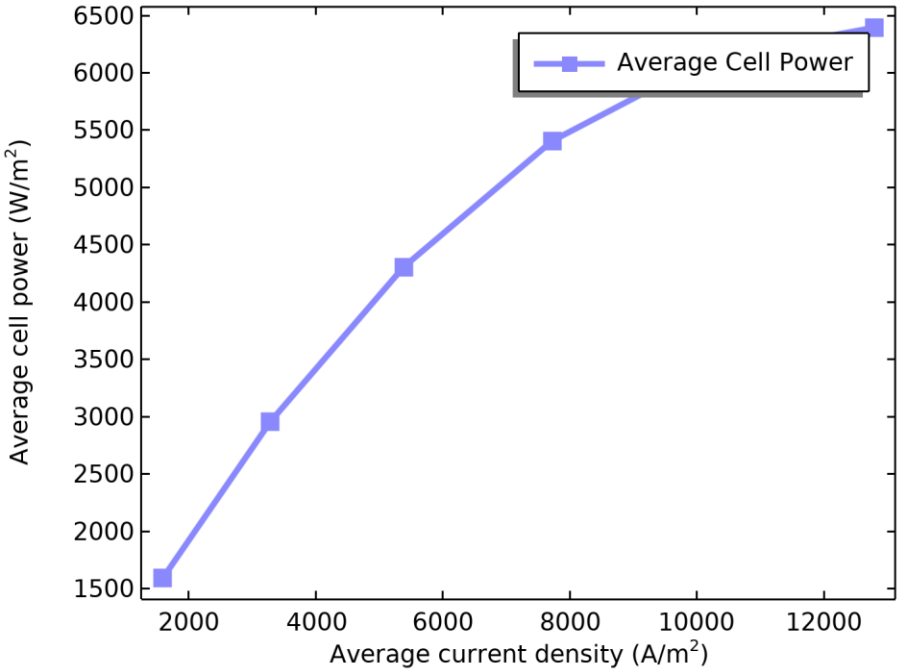

Figure IV.12. Current density and power density curves of the SOFC for CH_4/H_2 Gas mixture.

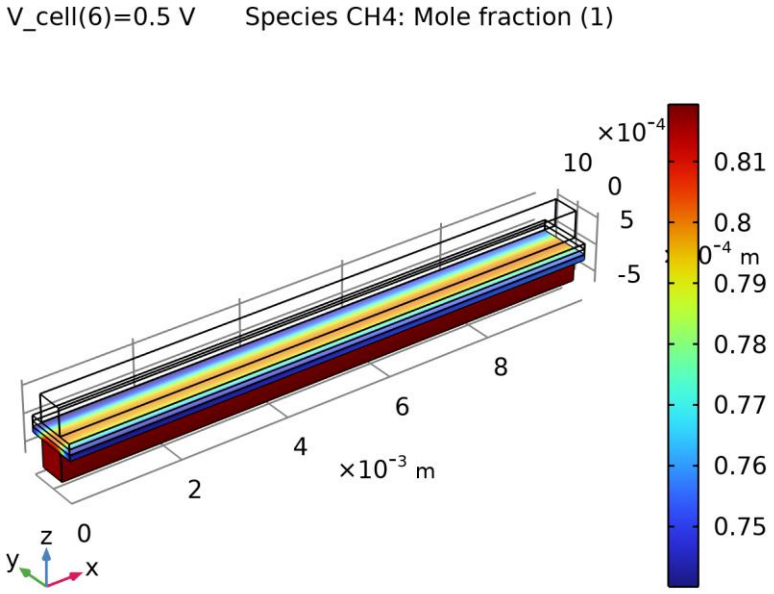

Figure IV.13. Methane mole fraction distribution in the anode gas channel at 0.5 V.

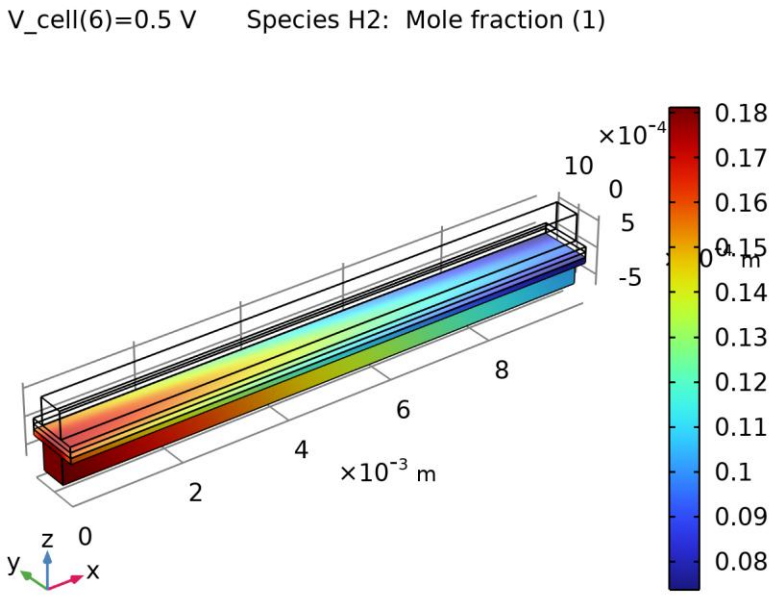

Figure IV.14. Hydrogen mole fraction distribution in the anode gas channel at 0.5 V.

For the CH_4/H_2 (70/30) mixture, the methane mole fraction remains nearly constant along the channel, while hydrogen decreases significantly (Figure IV.13, IV.14). Methane is not directly electrochemically oxidized in the model and cannot contribute to current generation without reforming. The declining hydrogen profile confirms that only the H_2 fraction is active electrochemically, leading to lower current density (Figure IV.15) compared with pure hydrogen. These distributions highlight the importance of internal or external reforming to convert CH_4 into H_2 before effective SOFC utilization.

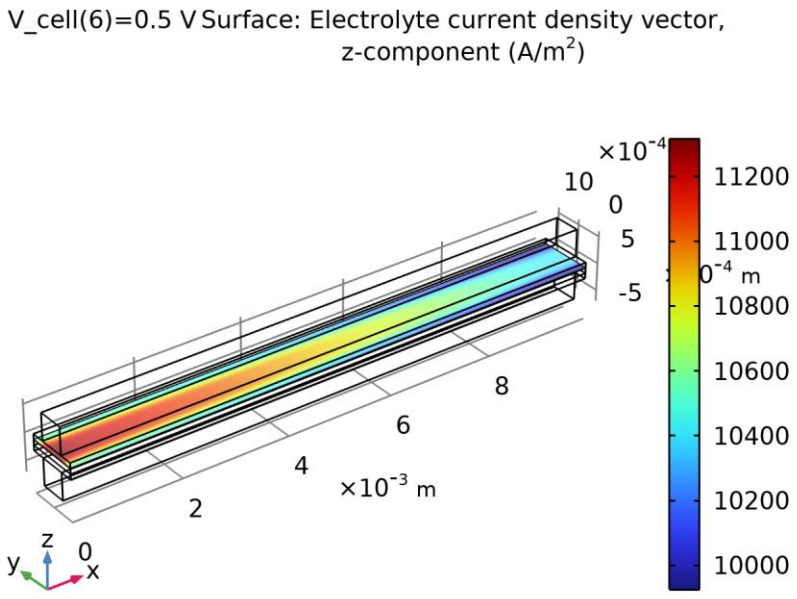

Figure IV.15. Electrolyte current density at 0.5 V.

IV.4 Conclusion

In this chapter, a detailed Multiphysics simulation of anode-supported SOFCs was presented, focusing on the effects of fuel composition and stoichiometry on electrochemical performance. The results confirmed the expected polarization behavior: activation losses were negligible, ohmic losses dominated, and concentration limitations became significant at high current densities or under fuel-lean conditions.

For hydrogen operation, stoichiometric feeding ($\lambda = 1$) caused strong fuel depletion and uneven current distribution. Moderate ($\lambda = 3$) and high ($\lambda = 5$) fuel excess improved cell stability and delayed concentration polarization. However, this came at the cost of reduced fuel utilization, as a larger fraction of hydrogen exited the anode unreacted.

When operating on methane–hydrogen mixtures, the model highlighted clear limitations. Methane remained largely unconsumed due to the lack of internal reforming, and only hydrogen contributed to current generation. These findings underscore the need for reforming reactions to achieve effective performance in methane-fed SOFCs.

IV.5 References

[1] Hussain, J., Ali, R., Akhtar, M. N., Jaffery, M. H., Shakir, I., & Raza, R. (2020). Modeling and simulation of planar SOFC to study the electrochemical properties. *Current Applied Physics, 20*(3), 414–422.

[2] Yakabe, H., Ogiwara, T., Matsuzaki, Y., & Yasuda, I. (2001). 3-D model calculation for planar SOFC. *Journal of Power Sources, 102*(1–2), 144–154.

[3] Singhal, S. C. (2000). Advances in solid oxide fuel cell technology. *Solid State Ionics, 135*(1–4), 305–313.

[4] Bessler, W. G., Gewies, S., & Vogler, M. (2007). A new framework for physically based modeling of solid oxide fuel cells. *Electrochimica Acta, 53*(4), 1782–1800.

[5] Aguiar, P., Adjiman, C. S., & Brandon, N. P. (2004). Anode-supported intermediate temperature direct internal reforming solid oxide fuel cell: II. Model predictions. *Journal of Power Sources, 138*(1–2), 120–136.

[6] Lan, R., Irvine, J. T. S., & Tao, S. (2012). Ammonia and related chemicals as potential indirect hydrogen storage materials. *International Journal of Hydrogen Energy, 37*(2), 1482–1494.

[7] Afif, A., Radenahmad, N., Cheok, Q., Shams, S., Kim, J. H., & Azad, A. K. (2016). Ammonia-fed fuel cells: A comprehensive review. *Renewable and Sustainable Energy Reviews, 60*, 822–835.

[8] Costamagna, P., & Honegger, K. (1998). Modeling of solid oxide heat exchanger integrated stacks and simulation at high fuel utilization. *Journal of Electrochemical Society, 145*(11), 3995–4007.

[9] Iwata, M., & Iwanari, T. (1996). Numerical simulation of planar-type solid oxide fuel cells. *Journal of Power Sources, 61*(1–2), 167–174.

[10] Virkar, A. V., Chen, J., Tanner, C. W., & Kim, J. W. (2000). The role of electrode microstructure on activation and concentration polarizations in solid oxide fuel cells. *Solid State Ionics, 131*(1–2), 189–198.

[11] Fuller, E. N., Schettler, P. D., & Giddings, J. C. (1966). New method for prediction of binary gas-phase diffusion coefficients. *Industrial & Engineering Chemistry, 58*(5), 18–27.

[12] Mason, E. A., & Malinauskas, A. P. (1983). *Gas Transport in Porous Media: The Dusty-Gas Model*. Elsevier.

General Conclusion

General Conclusion

This work is part of the broader context of hydrogen production and utilization for clean energy applications. The thesis addresses two complementary technologies: dielectric barrier discharge (DBD) plasma for hydrogen generation from methane, and solid oxide fuel cells (SOFCs) for efficient electrochemical conversion of hydrogen into electricity. The main objective was to develop numerical models providing insight into plasma-driven methane conversion and SOFC performance under different fuel compositions and operating conditions.

To achieve this, a fluid-type simulation model of non-equilibrium plasma was implemented, focusing on electron–molecule collisions, transport coefficients, and reaction kinetics in methane and argon/methane mixtures. The analysis identified the dominant reaction pathways leading to hydrogen formation and demonstrated how varying gas composition affects conversion efficiency and selectivity. In parallel, a COMSOL Multiphysics model of an SOFC unit cell was developed to simulate polarization and power density curves, evaluate ohmic and mass transport losses, and assess the impact of varying stoichiometry factors (λ) on fuel utilization and cell stability.

The results showed that plasma discharges can effectively decompose methane into hydrogen-rich syngas with limited CO_2 formation, highlighting the potential of DBD as a low-temperature hydrogen production route. On the fuel cell side, simulations confirmed that ohmic resistance is the dominant loss mechanism, while mass transport limitations become significant under stoichiometric operation ($\lambda = 1$). Increasing the stoichiometry factor improved current density and delayed concentration losses but reduced overall fuel utilization, illustrating the trade-off between efficiency and operational stability.

The work carried out opens the way to several perspectives. Among them:

- Extending the plasma model to more complex mixtures such as CH_4/CO_2 or CH_4/NH_3 to evaluate hydrogen yield and carbon management.
- Integrating thermal effects and degradation mechanisms into the SOFC model for more realistic long-term performance prediction.

- Investigating system-level coupling of plasma reactors and SOFC stacks, including heat and mass integration, to assess overall efficiency.
- Validating the models with experimental data to bridge the gap between simulation and practical implementation.

Overall, this thesis contributes to the understanding of plasma-assisted hydrogen production and electrochemical conversion in SOFCs, reinforcing the role of advanced numerical modeling in the development of sustainable hydrogen energy technologies.